

CENTRALE LANDBOUWCATALOGUS



0000 0086 5531

Promotor : dr.ir. L. Wartena, hoogleraar in de landbouwweerkunde
en de omgevingsnatuurkunde

Co-promotor : ir. J.A. Wisse, hoogleraar in de leer van het
buitenklimaat i.h.b. in verband met
de toepassing in de bouwkunde aan
de Technische Hogeschool Eindhoven

AN08201, 891

Pieter Jacobs

**The thermal behaviour of a three-dimensional
object placed in the open field**

Proefschrift
ter verkrijging van de graad van
doctor in de landbouwwetenschappen,
op gezag van de rector magnificus,
dr. C.C. Oosterlee,
hoogleraar in de veeteeltwetenschap,
in het openbaar te verdedigen
op vrijdag 23 april 1982
des namiddags te vier uur in de aula
van de Landbouwhogeschool te Wageningen.

15/16008201

STELLINGEN

I

Experimenteel bepaalde relaties tussen atmosferische grootheden hangen sterk af van de samenstelling van de atmosfeer en dienen derhalve met de grootst mogelijke voorzichtigheid te worden toegepast.

dit proefschrift

II

Bij de ontwikkeling van meetapparatuur dient meer rekening te worden gehouden met de omstandigheden waarin deze later gebruikt gaat worden.

dit proefschrift

III

Het is niet alleen opvallend doch tevens verbazingwekkend te constateren dat er in een tijd van energieschaarste nauwelijks metingen zijn verricht van het convectief warmte transport van gebouwen.

dit proefschrift

IV

Het streven naar eenduidige terminologie in het stralingsvakgebied heeft geleid tot talloze begrippen die op zichzelf weliswaar correct, doch als taal verwarring en onvolledig zijn.

V

Het quantificeren van stofeigenschappen in uitdrukkingen als 'de reflectie-coëfficiënt van gras', heeft alleen dan betekenis als de toestand waarin die stof zich bevindt nader wordt gespecificeerd.

VI

De energie-besparende werking van het verpakkingsmateriaal 'aircap', dat als isolatiemateriaal wordt gebruikt in tuinbouwkassen kan aanzienlijk worden verbeterd door het aanbrengen van een infrarood reflecterende coating.

VII

Voor een betere interpretatie van informatie verkregen m.b.v. remote sensing is het noodzakelijk dat er in de diverse onderwijsprogramma's meer aandacht wordt besteed aan de fysische aspecten.

VIII

Ondanks de soms enorme bezuinigingen op researchgelden dient erop toegezien te worden dat er voldoende middelen beschikbaar blijven voor het uitoefenen van vrije research.

IX

Het gevaar dreigt dat, indien de natuurlijke energiebronnen uitgeput raken, kernenergie met verhoogde risico's zal worden ingevoerd.

X

Om een daling van de werkloosheid te bewerkstelligen zal er naast het scheppen van werkgelegenheid gezorgd moeten worden voor het behoud van de bestaande werkgelegenheid.

Stellingen bij het proefschrift van P.A.M. Jacobs, getiteld:
'the thermal behaviour of a three-dimensional object placed in the open field'

Wageningen, 23 april 1982.

Aan mijn ouders

C O N T E N T S

Samenvatting/Summary

List of symbols

1.0 INTRODUCTION

2.0 DEFINITION OF THE PROBLEM

3.0 PROBLEM ANALYSIS

- 3.1 Shortwave irradiance from the upper hemisphere
- 3.2 Longwave irradiance from the upper hemisphere
- 3.3 Emitted radiation
- 3.4 Radiation exchange with the surrounding terrain
- 3.5 Convective heat exchange
- 3.6 Heat flow through the obstacle walls
- 3.7 Infrared detection

4.0 EXPERIMENTS

4.1 Experimental set-up

4.2 Instrumentation

- 4.2.1 Measurement of short- and longwave 'sky'-radiance
- 4.2.2 Net-radiometer
- 4.2.3 Heat flow sensor
- 4.2.4 Scanning radiometer 'ELSCA'
- 4.2.5 Infrared-reflectometer
- 4.2.6 Meteorological measurements

- 4.3 Data acquisition
- 4.4 Infrared imagers

5.0 ANALYSIS OF DATA AND RESULTS

5.1 Summary of performed measurements

5.2 'Sky'-radiance distribution

5.2.1 Shortwave irradiance

5.2.2 Longwave irradiance

- 5.3 Convective heat exchange
- 5.4 Radiative characteristics

6.0 CONCLUSIONS AND RECOMMENDATIONS

REFERENCES

Acknowledgements/Curriculum vitae

SAMENVATTING

In dit proefschrift zal worden ingegaan op de energie-uitwisseling tussen de atmosfeer en een drie-dimensionaal obstakel geplaatst in het vrije veld.

Deze problematiek maakt deel uit van een onderzoek dat wordt uitgevoerd binnen de groep Ver Infrarood van het Physisch Laboratorium TNO en dat gericht is op de discriminatie van objecten en hun omgeving in het infrarood golflengte gebied.

Na een korte inleiding en een omschrijving van de doelstelling worden in hoofdstuk 3.0 de verschillende warmteoverdrachtsprocessen besproken. Er wordt bekeken in hoeverre bestaande relaties te gebruiken zijn voor een dergelijk obstakel.

Omdat het niet mogelijk bleek te zijn met bestaande apparatuur alle termen in de warmtebalans experimenteel te bepalen, is een aantal apparaten ontwikkeld en gebouwd, die in hoofdstuk 4.0 worden besproken.

Deze apparaten zijn:

1. een Hemel Distributie Scanner ('HDS'); dit apparaat bepaalt de radiantie-verdeling van de hemel in het kort- en langgolvig spectraal gebied. Met behulp hiervan wordt de irradiantie van een horizontaal en een verticaal vlak bepaald.
2. een Elevatie SCanner ('ELSCA'); dit apparaat meet vanaf een platform de schijnbare emittantie van het obstakel en het omliggende terrein.
3. een infrarood reflectiometer; dit apparaat meet de infrarood reflectie van een oppervlak in verschillende golflengtegebieden. De meettijd is ca. 1 minuut.
4. twee vliegtuigscanners: een lijnscanner ('FLORIS') en een scanner met een cirkelvormig scanpatroon ('CIRCLE'). Beide kunnen gemonteerd worden in het vliegtuig van het International Training Centre (ITC) te Enschede.

Voor het testen van deze apparatuur zowel individueel als in samenhang met andere is een proefopstelling gebouwd op het vliegveld 'De Peel', gelegen in de provincie Limburg ten zuiden van Volkel.

De resultaten van deze testperiode worden besproken in

hoofdstuk 5.0. In dit hoofdstuk worden tevens de eerste resultaten van de metingen besproken.

Conclusies en aanbevelingen worden gegeven in hoofdstuk 6.0.

SUMMARY

In this thesis the energy-exchange between the atmosphere and a three-dimensional obstacle, placed in the open field is studied.

This problem is part of a research program carried out by the infrared group of the Physics Laboratory TNO and is mainly concerned with the discrimination of objects and backgrounds in the infrared region.

After a short introduction and a definition of the problem, chapter 3.0 is dealing with the heat exchange processes involved i.e. short- and longwave radiation, conduction and convective heat exchange. It is checked to what extent existing (empirical) relations can be used for such an obstacle.

Because it appeared not possible to measure all terms in the heat balance equation, a number of instruments has been developed and built and will be discussed in chapter 4.0. These instruments are:

- a. a sky-radiance distribution scanner ('HDS'); this instrument measures the short- and longwave radiance distribution of the sky with a spatial resolution of $15^{\circ} \times 15^{\circ}$.
From these measurements the irradiance at a horizontal- and vertical surface is determined.
- b. an elevation scanner ('ELSCA'); located on a platform this instrument measures the apparent emittance of the obstacle and the surrounding terrain.
- c. an infrared reflectometer; this instrument measures the infrared reflectivity of a surface in different wavelength bands. Measuring time 1 minute.
- d. to observe the scene from the air, two airborne scanners were used, a line scanner ('FLORIS') and a scanner having a circular scan pattern ('CIRCLE'). Both are mounted in the airplane of the International Training Centre (ITC) located at Enschede.

To test the instruments individually as well as in relation to the others, an experiment was carried out at the airfield 'De Peel', located in the province of Limburg.

The results of the system performance and of the first measurements are given in chapter 5.0.

Conclusions and recommendations are given in chapter 6.0.

LIST OF SYMBOLS

a	constant	
A	surface area	m^2
b	obstacle width	m
	constant	
c	cloud coverage	
	constant	
d	thickness of the obstacle walls	m
D	diffuse shortwave radiation	$\text{W} \cdot \text{m}^{-2}$
e	water vapor pressure	mbar
E	spectral emittance	$\text{W} \cdot \text{m}^{-2}$
f	spectral transmissivity of a filter	
F	view factor	
g	relative spectral responsivity	
G	apparent emittance	$\text{W} \cdot \text{m}^{-2}$
h	heat exchange coefficient	$\text{W} \cdot \text{m}^{-2} \cdot \text{K}^{-1}$
	obstacle height	m
	flight level	m
H	transfer function	$\text{V} \cdot \text{m}^{-2} \cdot \text{W}^{-1}$
K	longwave sky-radiance	$\text{W} \cdot \text{m}^{-2} \cdot \text{sr}^{-1}$
l	obstacle length	m
L	longwave radiation	$\text{W} \cdot \text{m}^{-2}$
	scaling length	m
M	shortwave sky-radiance	$\text{W} \cdot \text{m}^{-2} \cdot \text{sr}^{-1}$
n	julian day	
p	local latitude	rad
	resolution element of a scanner	m
Q	energy flux	$\text{W} \cdot \text{m}^{-2}$
R	distance	m
	random number	
S	shortwave radiation	$\text{W} \cdot \text{m}^{-2}$
t	time	s
T	absolute temperature	$^{\circ}\text{K}$
v	windspeed	$\text{m} \cdot \text{s}^{-1}$
	flight speed	$\text{m} \cdot \text{s}^{-1}$
V	voltage	V
W	spectral emittance of a black body	$\text{W} \cdot \text{m}^{-2} \cdot \mu\text{m}^{-1}$
x,y,z	space coordinates	m

Super- and subscripts

a	ambient/atmospheric
as	radiative, sky
b	black body
d	detector
el	elsca
f	feature
g	global
h	horizontal
i,j	index
ℓ	longwave
m	minimum
n	normal
N	net
p	pupil
s	surface/shortwave
t	total/terrain
v	vertical
w	tungsten

Non dimensional groups

N_{Re}	Reynolds number
N_{Nu}	Nusselt number

Greek alphabet

α	absorptivity	
	constant	
β	constant	
δ	sun's declination	rad
	constant	
ϵ	emissivity	
η	overlap	
θ	radiative temperature	K
κ	thermal diffusivity	$m^2.s^{-1}$
λ	thermal conductivity	$W.m^{-1}.K^{-1}$
μ	wavelength	μm

ν	kinematic viscosity	$\text{m}^2 \cdot \text{s}^{-1}$
ν_s	solar incident angle	rad
ρ	reflectivity	
σ	Stephan-Boltzmann constant	$\text{W} \cdot \text{m}^{-2} \cdot \text{K}^{-4}$
τ	transmissivity	
ϕ	azimuth angle	rad
ψ	elevation angle	rad
ω	hour angle	rad
	angular speed	$\text{r} \cdot \text{s}^{-1}$
Ω	solid angle	sr
Ω_s	solar constant	$\text{W} \cdot \text{m}^{-2}$

Acronyms used

HDS Hemel Distributie Scanner, a device scanning the sky and determining the shortwave- and longwave radiance distribution.

ELSCA Elevation SCanner, a device scanning the terrain from an elevated position and determining the apparent emittance of different features.

FLORIS } infrared line scanner (IRLS)
ORPHEUS }

CIRCLE infrared scanner with a circular scan pattern

Radiation conventions

shortwave $0.3 \leq \mu \leq 3 \text{ } \mu\text{m}$
longwave $3 < \mu \leq 50 \text{ } \mu\text{m}$

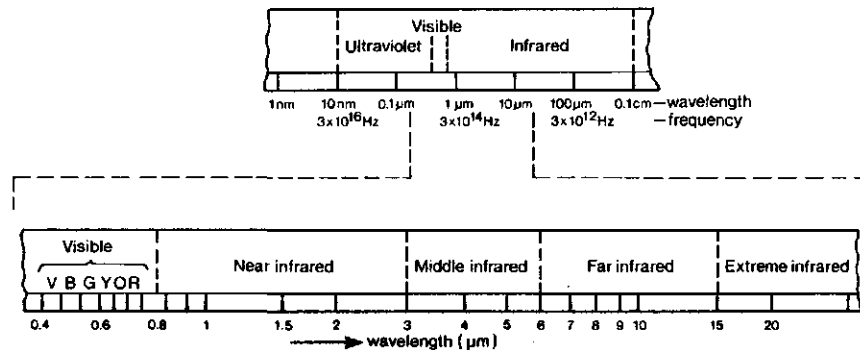
1.0 INTRODUCTION

Due to both the improvement of existing technology and development of new technology, new measurement-techniques are being introduced.

One of these techniques, called remote sensing, measures radiative properties of a surface, without disturbing existing local processes.

One of the most familiar sensors in this respect is the human eye, a unique sensor having characteristics of which some are still very hard to realize with an artificial sensor.

The disadvantage of this sensor however is the limited operation, due to a very small spectral sensitivity (fig. 1.1) followed by a subjective judgement of what is seen. It will be difficult to avoid this (except for full-automatic systems), for in many cases the human eye is the last link in a measuring cycle.



wavelength in vacuum

figure 1.1. The electromagnetic spectrum.

In most systems the sensor measures incident radiation and converts this to a voltage.

In the case of infrared-radiation the spectral radiant emittance of a surface is given by:

$$E_s(\mu, T_s) = \varepsilon_s(\mu) W(\mu, T_s) \quad (W \cdot m^{-2}) \quad (1.1)$$

$$W(\mu, T_s) = c_1 \mu^{-5} \left[\exp\left(\frac{c_2}{\mu T_s}\right) - 1 \right]^{-1} \quad (W \cdot m^{-2} \cdot \mu m^{-1})$$

wherein $W(\mu, T_s)$ black body spectral $(W \cdot m^{-2} \cdot \mu m^{-1})$
 $\varepsilon_s(\mu)$ spectral emissivity

c_1, c_2 radiation constants

$c_1 = 3.7415 \cdot 10^8 \quad (W \cdot m^{-2} \cdot \mu m^{-4})$

$c_2 = 1.4388 \cdot 10^4 \quad (\mu m \cdot K)$

μ wavelength (μm)

T_s surface temperature (K)

Figure 1.2 shows the spectral radiant emittance of a black body ($\varepsilon_s(\mu) = 1$) as a function of wavelength at various temperatures. The maximum spectral radiant emittance at a given temperature falls on the dashed curve (Wien's law, section 3.7).

A body whose emissivity ε_s is independent of wavelength is known as a *grey* body and many materials are approximately grey; a surface is called a *black body* when $\varepsilon_s = 1$ (maximum emission).

Integration of eq. 1.1 over the whole spectrum for a grey body leads to the *Stephan-Boltzmann* equation known as:

$$\varepsilon_s \int_{\mu=0}^{\infty} W(\mu, T_s) d\mu = \varepsilon_s \sigma T_s^4 \quad (W \cdot m^{-2}) \quad (1.2)$$

wherein σ *Stephan-Boltzmann constant* $(W \cdot m^{-2} \cdot K^{-4})$

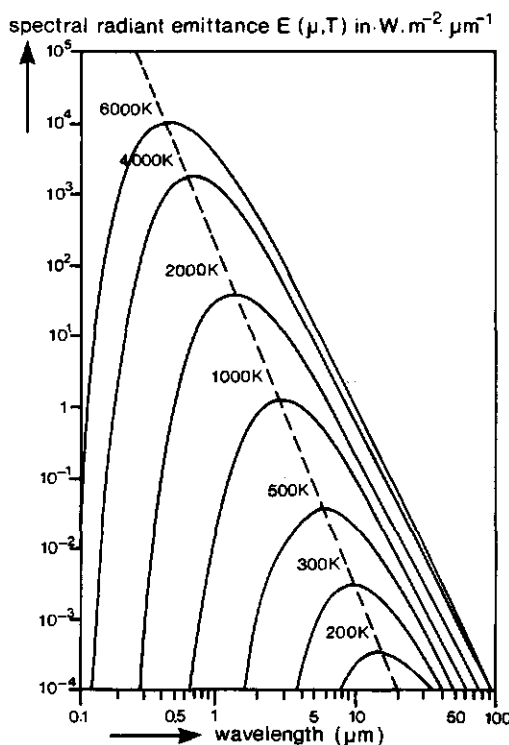
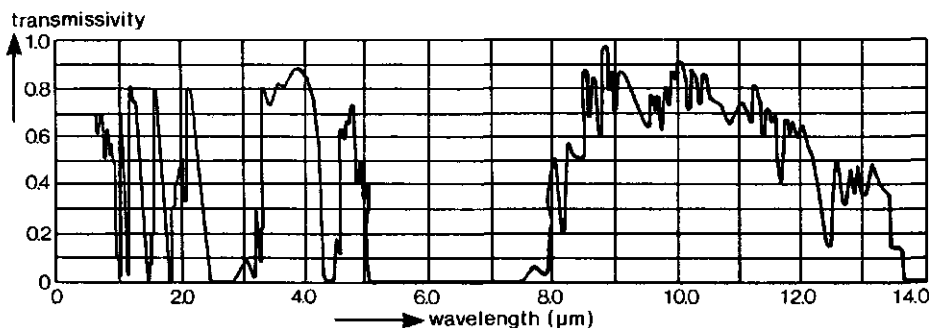


figure 1.2. Spectral radiant emittance of a black body as a function of wavelength at various temperatures.

To study the possibilities of remote sensing in the infrared (IR) region it is necessary to study atmospheric transmission and the emittance of a body. Equation 1.2 shows that the emittance is expressed in terms of the surface temperature and -emissivity [8, 9]. The emissivity is determined by surface properties and in many cases given by nature. Infrared atmospheric transmission τ_a is mainly determined by the amount of water vapor, carbon dioxide, aerosols and scattering. Figure 1.3 gives an example, showing two main transparent windows i.e. 3-5 μm and 8-14 μm . This explains why most IR-equipment used for remote sensing are operating in these wavelength bands.



Transmissivity for a 2 km path at sea level containing 17 mm of precipitable water [39]

figure 1.3. Atmospheric transmission.

In [17] a model is given to calculate IR-atmospheric transmission; measurements show [26, 27, 28] a general agreement with predicted values.

Using IR-equipment for remote sensing in a general sense poses some questions concerning the device- as well as the target characteristics; the most important one's are:

a. *device*

Is the device capable of performing a specific task?
This question is related to system geometrical- and temperature resolution.

b. *atmosphere*

What is the influence of atmospheric attenuation?

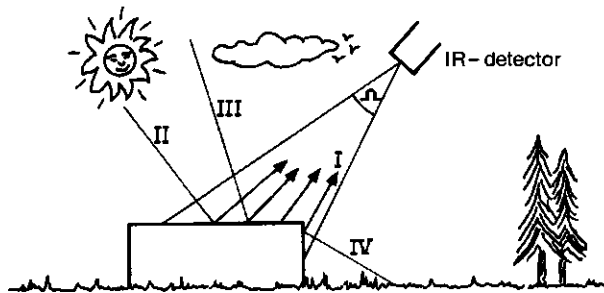
c. *object and background*

Is there a detectable IR-contrast between target elements or between target and background?

In practice equipment designers (answering a) are guided by the answer(s) to c.

Technically speaking almost any specification can be met in practice, like resolutions of 0.1 mrad or 0.01 K [29, 30]. However, whatever the specifications may be, if there is no contrast or the atmospheric transmission is very small (dense fog), IR-detection is not possible.

To find an answer to c it is necessary to determine the origin of the detected radiation (fig. 1.4).



- Ω field of view of an IR-system
- I surface emittance
- II reflected shortwave radiation
- III reflected longwave sky-radiation
- IV reflected longwave radiation emitted by the surrounding terrain

figure 1.4. Radiation incident on an IR-detector.

The detected radiation is determined by the apparent emittance G of a surface and the atmospheric transmissivity τ_a . The apparent emittance of a surface is the radiated energy, composed of emittance and longwave reflectance. In most cases the surface emittance contributes most to the apparent emittance, consequently G is determined by the surface emissivity and -temperature; the latter one is determined by the boundary conditions of the surface expressed as

$$\sum_i Q_i = 0 \quad (1.3)$$

Where Q_i are heat-transfer processes:

- Q_1 : absorbed shortwave radiation
- Q_2 : absorbed longwave atmospheric radiation
- Q_3 : radiation emitted by the surface
- Q_4 : absorbed radiation received from the surrounding terrain
- Q_5 : convective heat exchange
- Q_6 : heat flow through the wall
(heat transfer by condensation and evaporation is neglected).

In the next section the problems concerned with the solution of equation 1.3 in a practical situation are treated.

2.0 DEFINITION OF THE PROBLEM

To study the possible use of IR-techniques for remote sensing, the infrared group of the Physics Laboratory TNO has started a research program; the aim of this program can be described by the following subtasks:

1. *Definition of the physical model*

The detection of objects in a natural background is the ultimate goal. The main interest is to study the energy budget of an object placed in the open field. To keep the geometry simple, the object has been given a block shape with dimensions $l, b, h = 4, 2, 2$ m (section 3.0). The surfaces are painted green, with a paint of known reflective properties (fig. 5.23).

2. *Definition of the physical processes involved*

For each surface of the obstacle the following processes are taken into consideration (eq. 1.3):

- a. absorption of shortwave radiation
- b. absorption of longwave atmospheric radiation
- c. surface emittance
- d. heat flow through the surface
- e. convective heat exchange

For the body chosen we have to deal with horizontal- and vertical surfaces, and consequently a differentiation in the processes has to be made.

Literature has to be searched for the existence of practical usable expressions for these processes.

3. *Equipment design and installation of a test facility*

Depending on the existence of measuring equipment for the processes mentioned in item 2, there may be a need for new instruments or for improved measurement techniques.

To check system performance of the individual system and of all instruments as a measurement unit a suitable proving ground has to be determined (and found).

4. Measurement campaign

Depending on the results of this test period, which may give rise to improvements of systems or to a change of the experimental set-up, a measurement program has to be defined and carried out.

Aim of this measurement program is to measure the processes under different atmospheric conditions. This period includes overflights with IR-scanners.

5. Analysis and conclusions

Finally evaluation of the measurements will take place. To compare the results with values listed in literature or to introduce new empirical expressions. To enlarge the applicability of such relationships it is tried to express these in simple measurable quantities; for instance those measured by a synoptic weather station.

After having consulted the available literature, the findings, concerning the subtasks mentioned before, can be summarized as follows:

Subtask 2: physical processes

a. shortwave radiation

Shortwave radiation (solar radiation) is composed of a direct- and diffuse component. In [18, 24] semi-empirical expressions for these components are given as a function of solar elevation and -azimuth [7].

Shortwave irradiance at a horizontal plane (global irradiance) is easily measured, for instance with a solarimeter. For a vertical surface the two components have to be measured separately. The direct component can be determined by for instance a pyrheliometer. The diffuse component is difficult to measure. In [24] an expression for the diffuse irradiance at a vertical surface related to that at a horizontal surface is derived for northern latitudes ranging from 32° to 48° .

b. longwave atmospheric radiation

Much research already has been carried out to study longwave atmospheric radiation [1, 26, 42]; clear skies

as well as cloudy skies are treated [3]. Again much emphasize is put on longwave irradiance at a horizontal plane. Not much information is available about longwave atmospheric irradiance at a vertical plane; mostly this component is taken half of the irradiance at a horizontal plane.

Since the *absorbing* radiation is needed, the short- and longwave radiative properties of a surface have to be known. In literature [3, 4, 23, 35] reflection- and absorption coefficients of many materials (man-made, living) are listed; expressions like 'green grass' and 'dry dark soil' appear and are very subjective of nature, so one has to be careful using them. For the irradiance at a vertical surface the radiative properties of the surrounding terrain are needed.

c. *surface emittance*

The surface emittance is determined by the surface temperature and -emissivity (eq. 1.2, fig. 1.2).

For detection purposes the emittance in a limited spectral band often is needed and therefore the emittance has to be known in the same spectral region.

d. *convective heat exchange*

For an obstacle like ours no reports are made in the literature consulted. In [31] convective heat exchange of a story building is studied. In [32] a comparative experiment is described wherein the heat transfer of spheres under windtunnel- and atmospheric conditions is measured. In the latter case convective heat transfer was much more effective.

Contradictory reports are given about the influence of atmospheric turbulence intensity.

Subtask 3: Equipment and test facility

a. *shortwave- and longwave atmospheric radiation*

To get more information about the irradiance at especially vertical surfaces, an instrument to determine the sky-radiance distribution, called 'HDS' has been developed. This device measures the shortwave- and longwave radiance

simultaneously by scanning the sky with a field of view of $15^{\circ} \times 15^{\circ}$. From these measurements shortwave irradiance- (direct and diffuse) and longwave irradiance at a surface of arbitrary orientation is determined.

b. *surface emittance*

To measure the apparent emittance of different surfaces a scanning radiometer has been developed (called 'ELSCA') with a field of view of $2^{\circ} \times 2^{\circ}$. From an elevated position it scans the obstacle and the surrounding terrain. Since the scatter in the radiative properties given in literature is large and because there is a need for the spectral radiative properties of different materials an IR-reflectometer has been developed. Measuring time is 1 minute.

c. *data handling*

A data acquisition system was built, using a 64-channel multiplexer controlled by a micro-processor. Data are stored on cassette-tape.

d. Convective heat transfer is determined by the difference between the net-irradiance at a surface and the heat flow through the surface. This net-irradiance is measured with a Funk radiometer bought from Middleton Instruments. Heat flow is measured with heat flow sensor bought from TPD-TNO.

A proving ground was found located at the airfield 'De Peel' in the province of Limburg. Coordinates of this airfield are

$5^{\circ}52' \text{ E longitude}$
 $51^{\circ}32' \text{ N latitude}$

The testprogram was carried out in the summer of 1981.

Subtask 4: Measurement campaign

The main measurement period is scheduled to start in the summer of 1982. The duration of this exercise provisionally has been scheduled for one year.

In this thesis subtasks 1 up to and including 3 will be discussed. The results of the main measurement program will be published in the near future.

3.0 PROBLEM ANALYSIS

In this chapter the different terms in the heat balance equation (1.3) will be studied in more detail [9].

For the obstacle chosen a differentiation is made between horizontal and vertical surfaces.

A bottom-corner of the obstacle is chosen as the origin O (fig. 3.1) of a cartesian coordinate system (x, y, z).

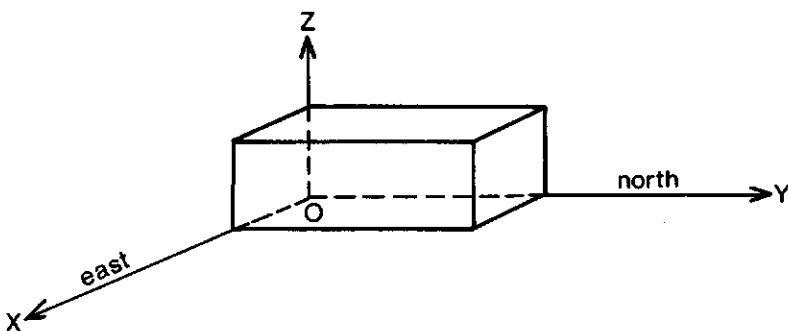


figure 3.1

These coordinates are related to the four quarters as:

- + x : east
- + y : north
- + z : zenith

The position of the sun is determined by its elevation angle ψ_s and azimuth angle ϕ_s related to the coordinate system as:

for ϕ_s :
 north $\equiv 0^\circ$
 east $\equiv 90^\circ$

for ψ_s :
 (x,y)-plane $\equiv 0^\circ$
 zenith $\equiv 90^\circ$

Similar for the wind direction ϕ_v :
 wind blowing from the north $\equiv 0^\circ$
 and from the east $\equiv 90^\circ$

3.1 SHORTWAVE RADIATION FROM THE UPPER HEMISPHERE

Shortwave radiation in this context is solar radiation in the spectral interval between 0.3 and 3 micrometer; the second boundary is chosen rather arbitrarily (cutoff wavelength of glass-hemispheres of a solarimeter).

Solar irradiance at the earth's surface depends on solar bearing and optical atmospheric properties.

Solar bearing [18] is given by two angles ψ_s and ϕ_s (fig. 3.2). From spherical trigonometry is known

$$\psi_s = \arcsin (\sin \delta \sin p + \cos p \cos \delta \cos \omega) \quad (\text{rad})$$

wherein δ solar declination

p local latitude

ω hour angle ($\omega = \phi_s - \pi$)

and

$$\phi_s = \arctan \left[\frac{\cos \omega}{(\sin p \cos \omega - \cos p \tan \delta)} \right] + \pi \quad (\text{rad})$$

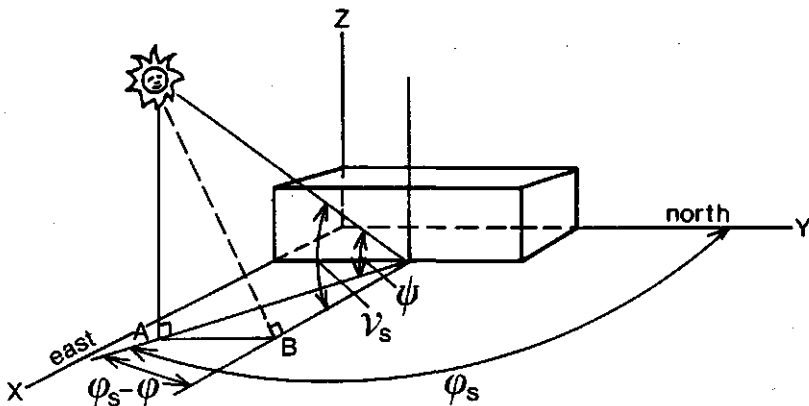


figure 3.2. Solar bearing.

The *solar incident angle* v_s i.e. the angle between the normal of a surface and the solar bearing is determined from:

- a. horizontal surface

$$v_s = \frac{\pi}{2} - \psi_s \quad (\text{rad})$$

- b. vertical surface

$$v_s = \arccos \left[\cos \psi_s \cos (\phi_s - \phi) \right] \quad (\text{rad})$$

wherein ϕ angle between north and the normal of a surface

Due to atmospheric scattering processes, solar radiation at the earth's surface consists of two components:

- a. A *direct* component i.e. solar-rays reaching the earth mainly without scattering.
- b. A *diffuse* component.

In practice both components have to be measured and afterwards the shortwave irradiance has to be calculated.

Two devices are often used in practice:

- a. A *pyrheliometer*.

It can be used to measure the direct irradiance S_n at normal incidence (narrow field of view, typical 5°).

- b. A *solarimeter*.

It measures the global irradiance S_g (direct + diffuse) at a horizontal plane.

For a horizontal surface the solarimeter readout can directly be used in the heat balance equation; for a vertical surface the irradiance has to be found from both measurements.

The *direct* component for a horizontal- and a vertical surface

is given by respectively:

$$S_h = S_n \sin \nu_s \quad (\text{W.m}^{-2})$$

and

$$S_v = S_n \cos \nu_s \quad (\text{W.m}^{-2})$$

In literature several experimental expressions are given. I used those found from measurements given in [18], valid for clear skies at northern latitudes ranging from 32° to 48° . The relation for S_n and the diffuse irradiance at a horizontal plane D_h reads:

$$D_h = \frac{1}{3}(\Omega_s - S_n) \sin \psi_s \quad (\text{W.m}^{-2})$$

wherein Ω_s the solar constant given by

$$\Omega_s = 1353 \left\{ 1 + 0.0338 \cos \left[\frac{2\pi}{365} (n - 3) \right] \right\} \quad (\text{W.m}^{-2})$$

with n the julian day

For the diffuse irradiance at a vertical plane D_v an experimental relation is determined [24] with D_h and ν_s as (fig. 3.3):

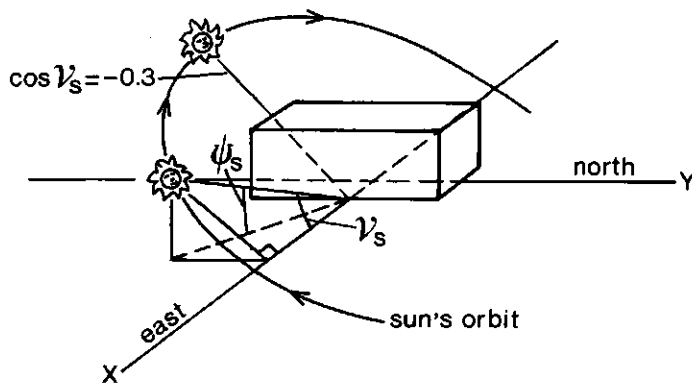


figure 3.3. Solar incident angle ν_s .

a. $\cos \nu_s \geq -0.3$

$$D_v = D_h (0.56 + 0.436 \cos \nu_s + 0.35 \cos^2 \nu_s) \quad (\text{W.m}^{-2})$$

b. $\cos \nu_s < -0.3$

$$D_v = D_h (0.473 + 0.043 \cos \nu_s) \quad (\text{W.m}^{-2})$$

Using a solarimeter (S_g), S_n can be found from:

$$S_n = \frac{3S_g - \Omega_s \sin \psi_s}{2 \sin \psi_s} \quad (\text{W.m}^{-2})$$

The relations mentioned are determined from 'clear sky' measurements and as already stated terms like these are of a very subjective nature because atmospheric transmission and emission may vary considerably (i.e. water vapor concentration, degree of pollution etc.).

As an example figure 3.4 shows own pyrheliometer- and solarimeter measurements and figure 3.5 shows derived parameters [9].

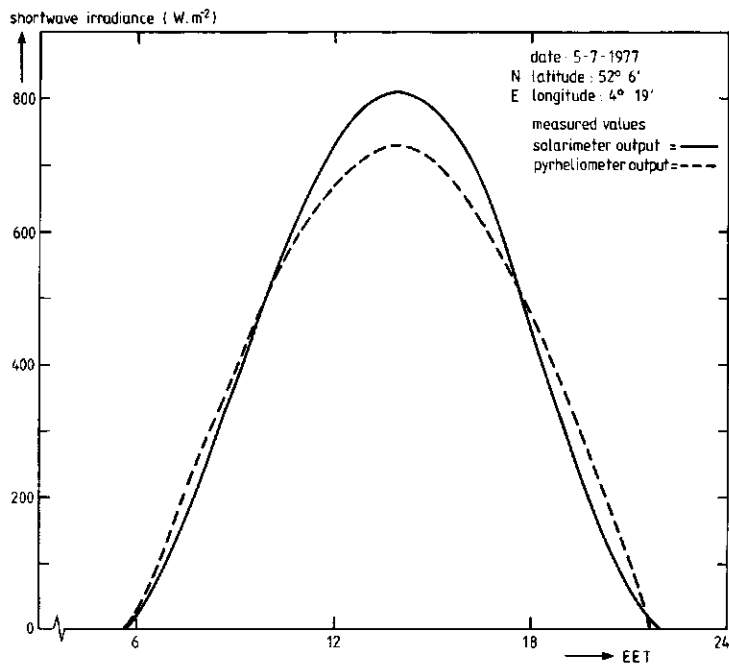


figure 3.4. Measured shortwave irradiance at normal incidence and measured global irradiance.

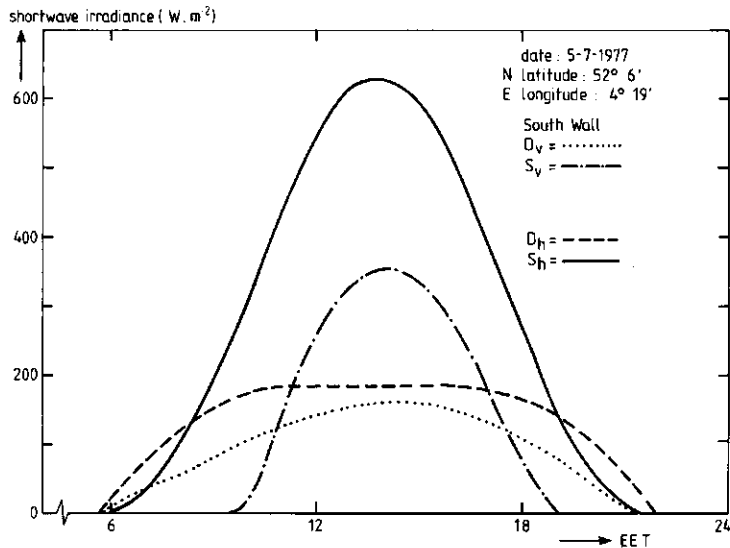


figure 3.5. Calculated shortwave irradiance at a horizontal surface and at a south facing vertical surface.

The amount of absorbed solar radiation Q_1 is

$$Q_1 = \bar{\alpha}_s \cdot X \quad (\text{W.m}^{-2}) \quad (3.0)$$

wherein $\bar{\alpha}_s$ mean solar absorptivity
 X solar-irradiance, depending on the orientation of the surface

Absorptivity can be wavelength- and/or angle dependent; this is determined by the nature of the surface [24].

Radiative properties of a surface like absorptivity, emissivity in equations like 3.0 are in fact integrated quantities found from:

$$\bar{\alpha}_s = \frac{\int \int \int \alpha_s(\mu, \psi, \phi) \sin \psi \cos \psi W(\mu, T(\psi, \phi)) d\psi d\phi d\mu}{\int \int \int \sin \psi \cos \psi W(\mu, T(\psi, \phi)) d\psi d\phi d\mu}$$

$$\text{wherein } \int \int \int \sin \psi \cos \psi W(\mu, T(\psi, \phi)) d\psi d\phi d\mu$$

wherein $T(\psi, \phi)$ spatial temperature distribution

In practice the spatial distribution of the radiative temperature T and α_s in the spectral band μ_o often is not known; in that case $\bar{\alpha}_s$ is calculated from

$$\bar{\alpha}_s = \frac{\int_{\mu_o} \alpha_s(\mu) W(\mu, T) d\mu}{\int_{\mu_o} W(\mu, T) d\mu}$$

For the spectral region

$0.3 < \mu_o < 3 \mu\text{m}$ T is of the order of 6000 K and for

$3 < \mu_o < 50 \mu\text{m}$ T is of the order of 300 K.

If the emissivity $\bar{\epsilon}_s$ is calculated the spectral emissivity $\epsilon_s(\mu)$ is weighted with Planck's function using the surface temperature T_s as radiation temperature i.e.

$$\bar{\epsilon}_s = \frac{\int \epsilon_s(\mu) W(\mu, T_s) d\mu}{\int W(\mu, T_s) d\mu} \quad (3 < \mu_o < 50 \mu\text{m})$$
$$\mu_o$$

3.2 LONGWAVE RADIATION FROM THE UPPER HEMISPHERE

In this context longwave radiation is within the spectral band 3-50 micrometer.

Longwave 'sky'-irradiance observed at the earth's surface is a results of a complicated process of emission and transmission of the atmosphere.

If a solid angle of the atmosphere has a mean emissivity $\bar{\epsilon}$ and a mean air temperature \bar{T} , the 'sky'-irradiance L at a surface can be found from

$$L = \frac{1}{\pi} \int_{\psi=0}^{2\pi} d\phi \int_{\mu_0}^{\frac{\pi}{2}} f(\psi, \phi) \bar{\epsilon}(\psi, \phi) W\{\mu, \bar{T}(\psi, \phi)\} d\psi d\mu \quad (\text{W.m}^{-2}) \quad \dots (3.1)$$

wherein $f(\psi, \phi)$ is a geometrical factor accounting for the surface orientation
 μ_0 spectral interval

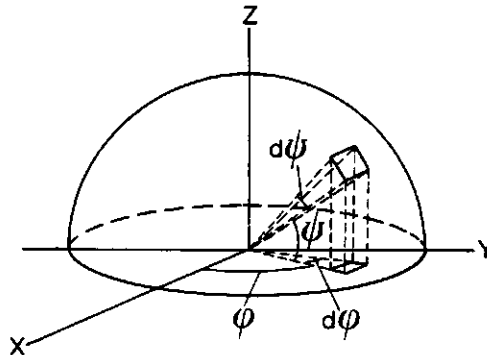


figure 3.6.

Again there is the difficulty that there is hardly any information available about $\bar{\epsilon}$ and \bar{T} as a function of meteorological conditions and as a function of bearing.

In practice eq. 3.1 is simplified by assuming that the atmosphere is a radiator at air temperature T_a (measured at screen height of approximately 1.5 m), having an *apparent emissivity* ϵ_a defined as

$$\epsilon_a(\psi, \phi) = \frac{\text{angular irradiance from a solid angle } (\psi, \phi)}{\text{emittance of a blackbody at air temperature}}$$

Rewriting eq. 3.1

$$L = \frac{1}{\pi} \int_{\phi=0}^{2\pi} d\phi \int_{\mu=0}^{\frac{\pi}{2}} \int_{\psi=0}^{\frac{\pi}{2}} f(\psi, \phi) \epsilon_a(\psi, \phi) W(\mu, T_a) d\psi d\mu \quad (\text{W.m}^{-2}) \quad \dots (3.2)$$

Under 'clear' sky conditions there is hardly any dependence of $\epsilon_a(\psi, \phi)$ on the azimuth angle ϕ [3, 25].

In [1, 3] an expression for $\epsilon_a(\psi)$ is given as a function of elevation ψ and water vapor pressure e

$$\epsilon_a(\psi) = a + b \sqrt{e} + c \ln[\sin(\psi)] \quad (3.3)$$

wherein e in mbar

a, b, c to be determined by experiment [3]

Solving eq. 3.2 for a horizontal- $\{f(\psi, \phi) = \sin \psi \cos \psi\}$ and a vertical surface $\{f(\psi, \phi) = \cos^2 \psi\}$ leads to:

$$L = \delta \sigma T_a^4 [\alpha + \beta \sqrt{e}] \quad (W.m^{-2}) \quad (3.4)$$

with $\delta = 1$ for a horizontal surface

$\delta = 0.5$ for a vertical surface

The experimental constants α and β depend on atmospheric properties.

The constants a , b and c in eq. 3.3 are related to the constants α and β in eq. 3.4 by:

$$a = \alpha - 0.5 \beta$$

$$b = \beta$$

$$c = -1.4728 \beta$$

In [3] table 2 shows values measured at different locations in England and the USA ranging from

$$(0.51, 0.065) < (\alpha, \beta) < (0.60, 0.059)$$

Mean values are given as $\alpha = 0.58$ and $\beta = 0.061$.

In [40] table 3 shows the variation of α and β during the year measured at Deelen, The Netherlands. The range of the coefficients here is

$$(0.60, 0.057) < (\alpha, \beta) < (0.75, 0.017)$$

annual mean values are $\alpha = 0.678$ and $\beta = 0.041$.

Mean values for α and β , using both resources are $\alpha = 0.63$ and $\beta = 0.051$.

The term between brackets in eq. 3.4 can be regarded as a mean apparent atmospheric emissivity $\bar{\epsilon}_a$

$$\bar{\epsilon}_a = \alpha + \beta \sqrt{e} \quad (3.5)$$

In practice often the term 'radiative temperature of the sky θ_{as} ' is used; in that case it is assumed that $\bar{\epsilon}_a = 1$ and $L = \sigma \theta_{as}^4$, using eq. 3.4 an expression for θ_{as} is found as

$$\theta_{as} = (\alpha + \beta \sqrt{e})^{0.25} T_a \quad (K) \quad (3.6)$$

numerical example:

relative humidity	0.7	
air temperature	293	(K)
water vapor pressure	16.4	(mbar)

If maximum and minimum values for α and β are used, these data result in

$$0.77 < \bar{\epsilon}_a < 0.82$$

$$0.93 T_a < \theta_{as} < 0.95 T_a \quad (K) \quad (3.7)$$

In [1, 3] an expression for $\bar{\epsilon}_a$ is given as a function of cloudcover as

$$\bar{\epsilon}_a(c) = (1 - 0.84 c) \bar{\epsilon}_a(0) + 0.84 c \quad (3.8)$$

$$\text{or } \bar{\epsilon}_a(c) = \bar{\epsilon}_a(0) (1 + kc^2)$$

wherein c fraction of cloud cover

$\bar{\epsilon}_a(0)$ emissivity under 'clear sky' conditions

k a factor, ranging from 0.2 for low cloud to 0.04 for high cloud.

The longwave irradiance at vertical surfaces depends on the radiation distribution of the sky; for 'clear sky' conditions eq. 3.4 is applicable with $\delta \approx 0.5$ while under cloudy conditions δ may vary considerably (except for a homogeneous cloud distribution).

The amount of absorbed atmospheric longwave radiation Q_2 (eq. 1.3) is

$$Q_2 = \delta \bar{\alpha}_L L \quad (\text{W.m}^{-2})$$

wherein $\bar{\alpha}_L$ absorptivity for longwave radiation
(section 3.1)

In [1, 4, 23] radiative properties are listed for different materials (man-made as well as living).

3.3 EMITTED RADIATION

As already mentioned in the introduction the emittance of a surface is determined by the surface temperature T_s and the emissivity $\epsilon_s(\mu)$ as

$$Q_3 = \int_{\mu=0}^{\infty} \epsilon_s(\mu) W(\mu, T_s) d\mu \quad (W \cdot m^{-2}) \quad (3.9)$$

Using a mean emissivity $\bar{\epsilon}_s$ (section 3.1) eq. 3.9 can be solved, leading to

$$Q_3 = \bar{\epsilon}_s \int_{\mu=0}^{\infty} W(\mu, T_s) d\mu = \bar{\epsilon}_s \sigma T_s^4 \quad (W \cdot m^{-2})$$

In airborne infrared imagers (section 4.4) often two spectral intervals are used [29], the so-called 5 and 10 μm window. In this case equation 3.9 is integrated over the spectral width μ_0 of the window.

3.4 RADIATION EXCHANGE WITH THE SURROUNDING TERRAIN

Vertical surfaces receive radiation (emitted, reflected) from the surrounding terrain.

Apart from the radiative properties of both areas, the radiation exchange is determined by the so-called view factor F_{ij} between area i and j (fig. 3.7).

This factor is defined as the fraction of the total emitted radiation (N_t) by surface i , which is directly incident on area j (N).

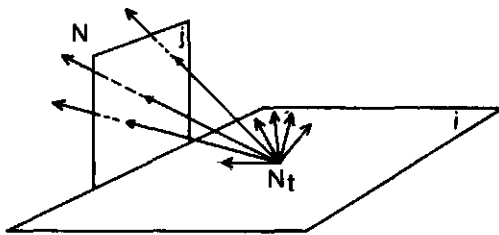


figure 3.7.

$$F_{ij} = \frac{N}{N_t}$$

The irradiance Q_4 (eq. 1.3) at area j then is (neglecting multiple reflections):

$$Q_4 = \bar{\alpha}_{j,s} F_{ij} D + \bar{\alpha}_{j,l} F_{ij} G \quad (\text{W.m}^{-2})$$

wherein $\bar{\alpha}_{j,s}$ and $\bar{\alpha}_{j,l}$ shortwave- resp. longwave absorptivity of surface j
 D diffusely reflected shortwave irradiance at surface i
 G apparent emittance of surface i (i.e. emitted + reflected radiation)

For very simple geometries the view factor can be determined from tables [4] or by formulas.

In the case of a three-dimensional obstacle, area's of irregular shape can exist on the underground (sunshadow, terrain inhomogeneity). In such a case the view factor is determined by a numerical method using a *monte carlo* technique (fig. 3.8).

The following steps describe the procedure

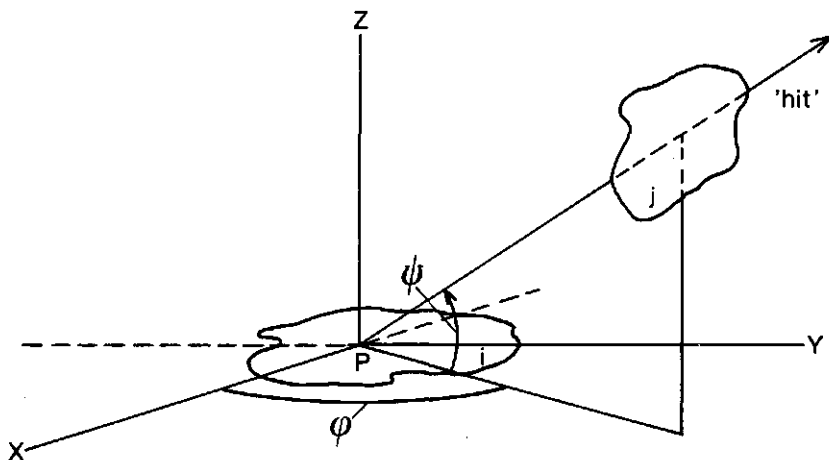


figure 3.8.

- a. select at random a point P within area i
- b. select at random a direction (ψ, ϕ) of an emitted ray from area i . The distribution of the emitted rays is made Lambertian by defining ψ and ϕ from two random numbers R_1 and R_2 as [12],

$$\phi = 2 \pi R_1 \quad (\text{rad})$$

$$\cos \psi = \sqrt{R_2} \quad 0 \leq R \leq 1$$

- c. determine whether this ray is intercepted by area j if yes, a 'hit' is counted
- d. repeat this procedure a great number of times (this number depends on the accuracy required)
- e. the view factor F_{ij} is determined by the ratio of the number of hits U_h and the total number of emitted rays U_t i.e.

$$F_{ij} = \frac{U_h}{U_t}$$

To study the influence of this radiation-exchange a parameter P is introduced being the radiation absorbed by area j (Q_4) due to this mechanism, divided by the *total* amount of radiation absorbed by area j ($Q_1 + Q_2 + Q_4$) i.e.

$$P = \frac{Q_4}{Q_1 + Q_2 + Q_4}$$

It is found [9] that P reaches values up to $P = 0.5$ during nighttime, meaning that there is a strong coupling between surface j and the surroundings. In [41] values for cylindrical vertical walls (e.g. evaporation pan and fuel tanks) values up to $P = 0.8$ were found.

3.5 CONVECTIVE HEAT EXCHANGE

The fundamental equation for the heat transfer between a surface at temperature T_s and a fluid in contact with it at temperature T_a is (eq. 1.3):

$$Q_5 = h (T_s - T_a) \quad (\text{W.m}^{-2})$$

wherein h heat exchange coefficient $(\text{W.m}^{-2}.\text{K}^{-1})$

The coefficient h is determined by geometry, fluid dynamics and fluid properties (in our case air).

The complication in this equation is the definition of the air temperature T_a . In this case T_a will be adopted as the air temperature measured at a screen height of 1.5 m at approximately 20 m away from the obstacle.

The state the fluid is in, can be expressed by dimensionless numbers, some of them derived from the Navier-Stokes equations and from the energy equation [2, 21]:

1. Reynolds number N_{Re}

$$N_{Re} = \frac{vL}{\nu}$$

wherein v windspeed of the arriving air (m.s^{-1})
 L scaling length (m)
 ν kinematic viscosity $(\text{m}^2.\text{s}^{-1})$

2. Nusselt number N_{Nu}

$$N_{Nu} = \frac{hL}{\lambda}$$

wherein λ thermal conductivity of air $(\text{W.m}^{-1}.\text{K}^{-1})$

From windtunnel experiments it is known that the airflow may be either *laminar* or *turbulent*; the transition between laminar and turbulent airflow is determined by the Reynolds number, however no sharp transition exists.

Convective heat exchange can be either *free* or *forced*; again no sharp transition exists.

In our case, dealing with an obstacle in the open field, the airflow always is turbulent and nearly always forced convection is the main heat exchange mechanism. From wind tunnel experiments it is known that in the case of turbulent flow and forced convection h is related to the Reynolds number. It is anticipated that under atmospheric conditions this is also the case.

The windspeed used in the Reynolds number is the windspeed measured at a height of 1.5 m at approximately 20 m away from the obstacle. Half the perimeter of a surface is used as scaling length.

It is also anticipated that the convective heat exchange coefficient, at least for vertical surfaces, depends on the wind direction ϕ_v [10]. Contradictory reports are given in the literature consulted about the influence of atmospheric turbulence intensity on the convective heat transfer. During the test period this parameter is not determined but will be measured during the measurement campaign.

In conclusion the convective heat exchange coefficient h in this thesis will be related to the Reynolds number N_{Re} and to the wind direction ϕ_v expressed by the function $f(\phi_v)$ i.e.

$$h = a N_{Re}^n f(\phi_v) \quad (W \cdot m^{-2} \cdot K^{-1})$$

$$\text{wherein } a \text{ a constant} \quad (W \cdot m^{-2} \cdot K^{-1})$$

3.6 HEAT FLOW THROUGH THE OBSTACLE WALL

One-dimensional heat conduction, neglecting boundary effects, is given by (eq. 1.3):

$$Q_6 = - \lambda \left(\frac{\partial T}{\partial z} \right)_{\text{surface}} \quad (\text{W.m}^{-2})$$

wherein λ thermal conductivity of the wall ($\text{W.m}^{-1}.\text{K}^{-1}$)
 z' local coordinate normal to the
surface (m)

3.7 INFRARED DETECTION

As already mentioned in the introduction an infrared detector converts incident longwave radiation to an output voltage V_d [39], in general form written as (fig. 3.9),

$$V_d = \int_{A_1} \int_{A_2} \frac{\cos \nu_d}{R^2} dA_1 dA_2 \int_{\mu_0} \frac{G_s(\mu, T_s)}{\pi} H(\mu) \tau_a(\mu) d\mu \quad (V) \quad \dots (3.10)$$

wherein	A_1	aperture of IR-system	(m^2)
	A_2	area of the observed surface	(m^2)
	R	distance between A_1 and A_2	(m)
	ν_d	bearing of the system	(rad)
	μ_0	spectral interval	(μm)
	H	detector transfer function	$(V \cdot W^{-1} \cdot m^2)$
	τ_a	atmospheric transmissivity	
	V_d	output voltage of the detector (V)	
	G_s	apparent emittance of the surface A_2 (p. 5)	$(W \cdot m^{-2})$

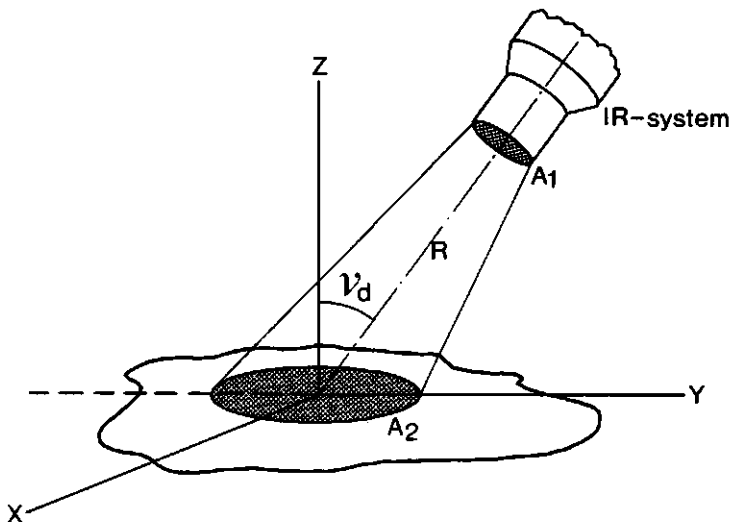


figure 3.9.

In many cases the surface emittance contributes most to the total incident radiation; only in special cases like low solar altitude (in the 3-5 μm spectral band), or using low emissivity paint ($\bar{\epsilon}_s = 0.50$) reflective parts may become important.

Since the solar radiation is rapidly decreasing with wavelength in the infrared region ($> 3 \mu\text{m}$), IR-detectors can also be used in daytime without much disturbing influence of the sun. To simplify equation 3.10 a geometrical fixed situation is assumed; then with the detector characteristics being given eq. 3.10 reduces to,

$$v_s = c \int_{\mu_0}^{\infty} \epsilon(\mu) W(\mu, T_s) H(\mu) \tau_a(\mu) d\mu \quad (\text{V}) \quad (3.11)$$

wherein c a constant incorporating the given geometry

Equation 3.11 clearly shows the relation between v_d and the surface properties ϵ_s and T_s .

Calibration of eq. 3.11 using a black body ($\epsilon_s = 1$) at a given set of temperatures T_b , at short distance from the IR-system ($\tau_a = 1$) leads to,

$$v_d = a \int_{\mu_0}^{\infty} W(\mu, T_b) d\mu + b \quad (\text{V}) \quad (3.12)$$

from which a and b can be determined.

Since in practice ϵ_s and T_s are not known eq. 3.12 is used differently,

$$v_d = a \left[\int_{\mu_0}^{\infty} W(\mu, \theta_s) d\mu \right] + b \quad (\text{V}) \quad (3.13)$$

wherein θ_s is the radiative temperature
defined as

$$\int_{\mu_0}^{\infty} \varepsilon_s(\mu) W(\mu, T_s) d\mu = \int_{\mu_0}^{\infty} W(\mu, \theta_s) d\mu \quad (3.14)$$

Thus, in this way the radiative temperature θ_s can be found; in many cases the emissivity will be close to unity and in that case $T_s \approx \theta_s$.

The next step is to move the spot (A_2) over the scene and to monitor the output voltage V_d (fig. 3.10).

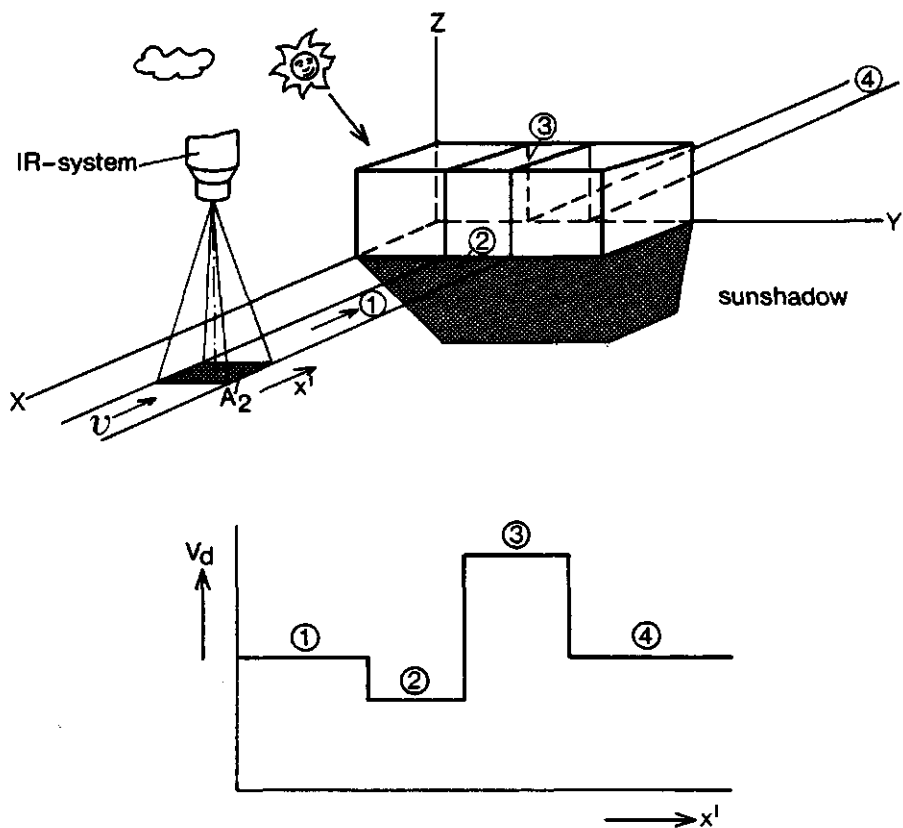
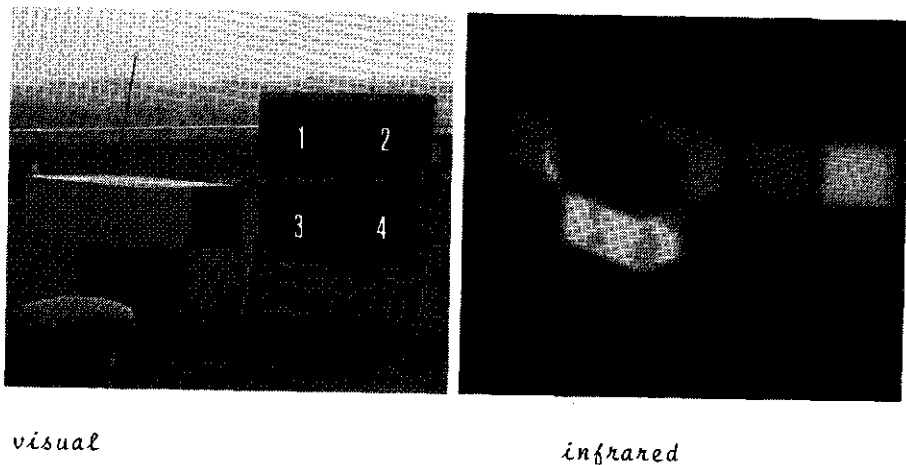


figure 3.10.

The different levels are caused by a difference in radiative temperature θ_s but as eq. 3.14 shows a difference in θ_s can be established through ϵ_s as well as through T_s i.e.,

$$\Delta V_d = \left(\frac{\partial V_d}{\partial \epsilon_s} \right)_{T_s} \Delta \epsilon_s + \left(\frac{\partial V_d}{\partial T_s} \right)_{\epsilon_s} \Delta T_s \quad (V)$$

Figure 3.11 shows two extremes i.e. T_s is constant while $\Delta \epsilon_s$ is large (left part) and ϵ_s is constant while ΔT_s is large (right part).



four panels to the right have temperatures of:

1. ambient (air) temperature T_a
2. $T_a + 1^\circ\text{C}$
3. $T_a + 2^\circ\text{C}$
4. $T_a + 5^\circ\text{C}$

The different patches on the box have different emissivities (and equal temperature).

figure 3.11.

The figure shows another way of displaying the results. In this case the voltage is used to burn a light emitting diode (LED); the light is exposed to a film negative (or monitored with a TV-camera). Thus a large luminance results in a deep blackening of the negative (i.e. large emittance). On a positive print like fig. 3.11 white areas are warmer than dark areas.

Due to atmospheric limitations (fig. 1.3) mostly two spectral bands are used in practice i.e. 3-5 μm and 8-14 μm .

Wien's law:

$$\mu_m = 2897/T_s \quad (\mu\text{m})$$

where μ_m wavelength of maximum emittance (μm)
 T_s surface temperature (K)

shows that for bodies at ambient air temperatures ($T_s \approx 300 \text{ K}$) $\mu_m \approx 10 \mu\text{m}$, while for hot bodies like exhaust pipes ($T_s \approx 700 \text{ K}$) $\mu_m \approx 4 \mu\text{m}$.

So, nature has given us a hand here.

4.0 EXPERIMENTS

Aim of the experimental trial is to study the thermal behaviour of an obstacle placed in the open field. This is done by measuring the different heat exchange processes at the interior- and exterior boundaries of the obstacle i.e.

- a. radiative heat exchange
- b. convective heat exchange
- c. heat flow through the wall

First part of this measurement program, which will be discussed in this thesis, is to test system performance i.e.

- a. testing system hardware (electronics, calibration)
- b. to investigate the meaning of the measured quantity by comparing measurements found from different measurement techniques
- c. to test the experimental set-up as a measurement unit.

To minimize costs three surfaces of the obstacle (the top-, the west- and north surface) are used as measuring surfaces. Figure 4.1 shows the orientation of the obstacle relative to north.

The test period started in the summer of 1981 and lasted until the late autumn of 1981. This period falls within the time wherein The Netherlands adopted East European Time (EET); GMT and EET are related by:

$$\text{EET} = \text{GMT} + 2 \text{ (hours)}$$

4.1 EXPERIMENTAL SET-UP

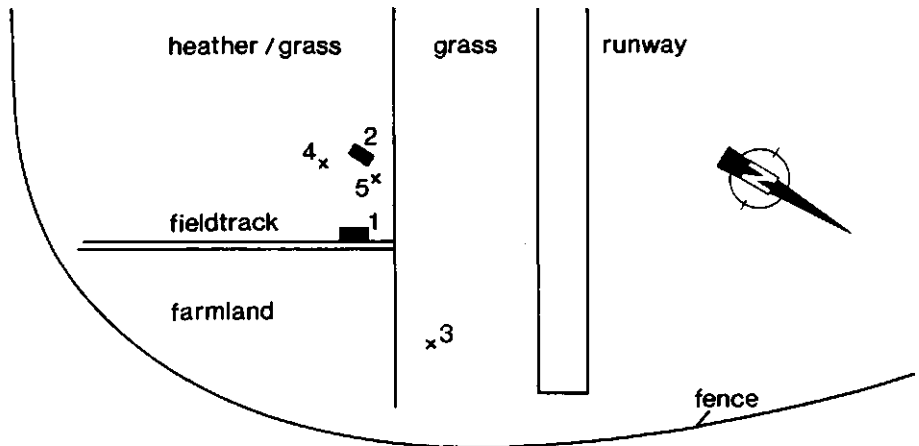
The experimental site was chosen in the north-east corner of the airfield 'De Peel', located in the province of Limburg, south of Volkel.

Coordinates of this airfield are:

5°52' E longitude

51°32' N latitude

The N-E corner was chosen because of the presence of electrical power in that area; consequently there is a homogeneous terrain in a sector: $270^\circ \pm 90^\circ$ about 1 km in length. In that direction the vegetation mainly consists of grass, but due to strict security regulations it was not possible to have equipment placed on it. It was, however, possible to use an adjacent heather field cut to a comparable height to that of the grass (fig. 4.1).



1. portacabine (painted white)
2. measuring area + obstacle (painted green)
3. power supply (meteo station of air basis)
4. platform
5. weather station

figure 4.1. Experimental area.

The size of the obstacle is: $l, b, h = 4, 2, 2$ (m).

Three sides of this block are used as measuring area's and are equipped with sensors. Each side is divided in elements of 1 m^2 , this is the smallest resolution element (fig. 4.2).

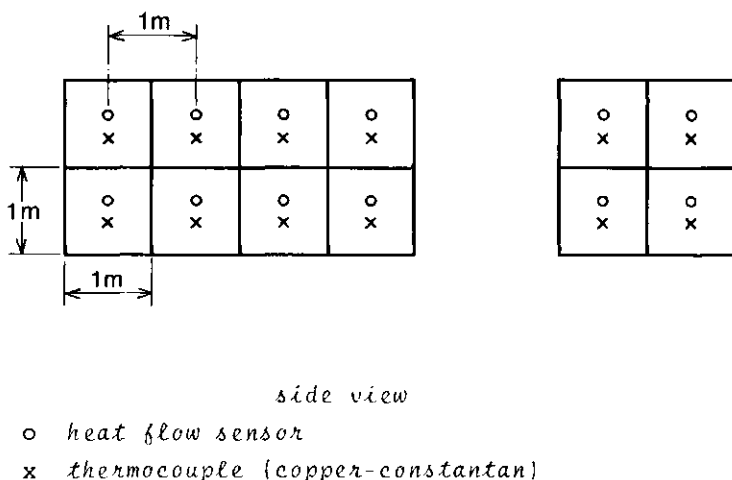


figure 4.2. Location of the heat flow sensors and thermocouples on the obstacle walls.

A more detailed picture of such an area is given in fig. 4.3.

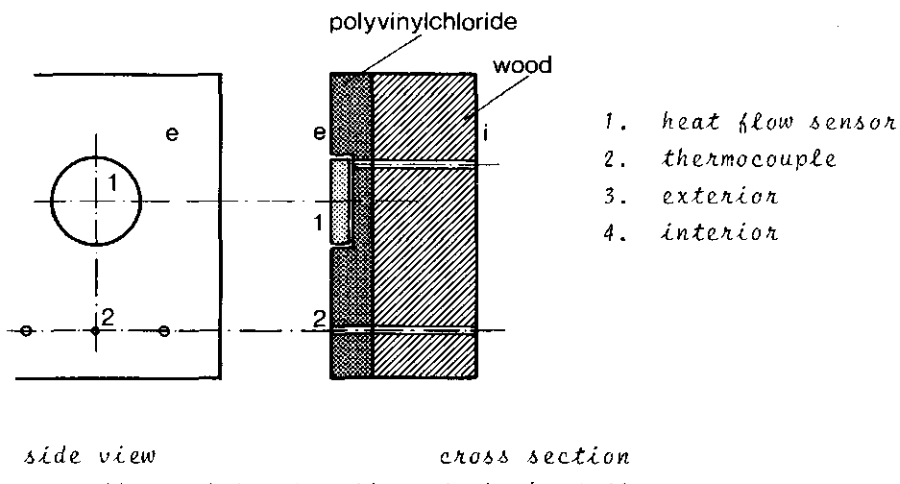


figure 4.3. Location of the heat flow sensors.

One large side of the obstacle is used and is pointed to the west; the second large one is the top surface; the small side is directed to the north (fig. 4.1).

Since the heat flow sensors merely consist of *polyvinyl-chloride* (PVC), the exterior surface of the obstacle is made of 6 mm PVC-plate, so the thermal conductivity and heat capacity of the PVC-plate and heatflow sensors are the same within 1%. The thermocouples are also placed in the PVC, just below the surface.

The entire external surface is painted green; the shortwave- and longwave properties of this paint are known.

In front of each selected measuring-side a sensor, measuring the net-irradiance, is placed (fig. 4.19).

If, both the heat flow through the surface Q_6 and the net-irradiance Q_N at the surface are known, the convective heat-exchange Q_5 is found from equation 1.3.

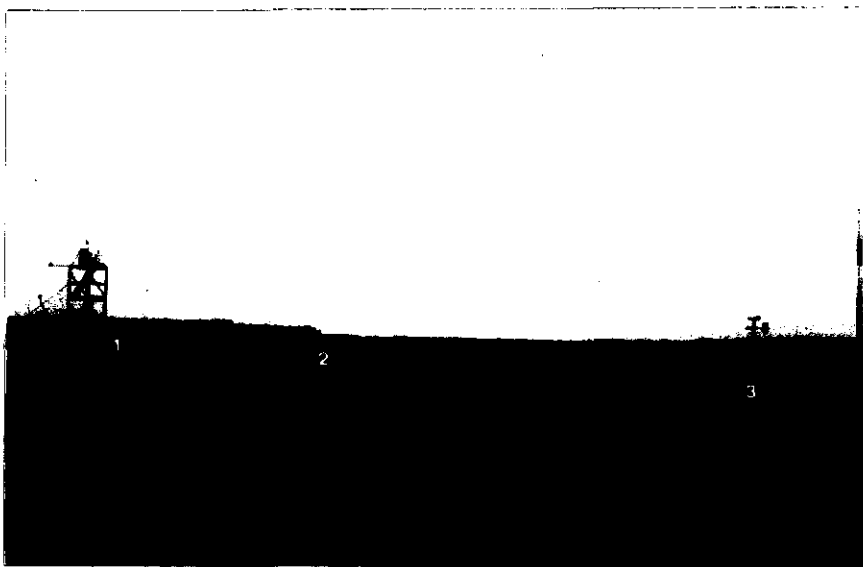
Next to the obstacle (± 14 m, fig. 4.4) a measuring platform is placed, which is elevated ± 7 m above ground level.

Two instruments are placed on this platform:

1. a scanning device measuring short- and longwave 'sky'-radiance as a function of azimuth and elevation (cf. 4.2.1) called 'HDS'; field of view is $15^\circ \times 15^\circ$.
2. another scanning device measuring the radiative-temperature of different land based targets, i.e. the obstacle and the surrounding terrain, called 'ELSCA'; field of view is $2^\circ \times 2^\circ$.

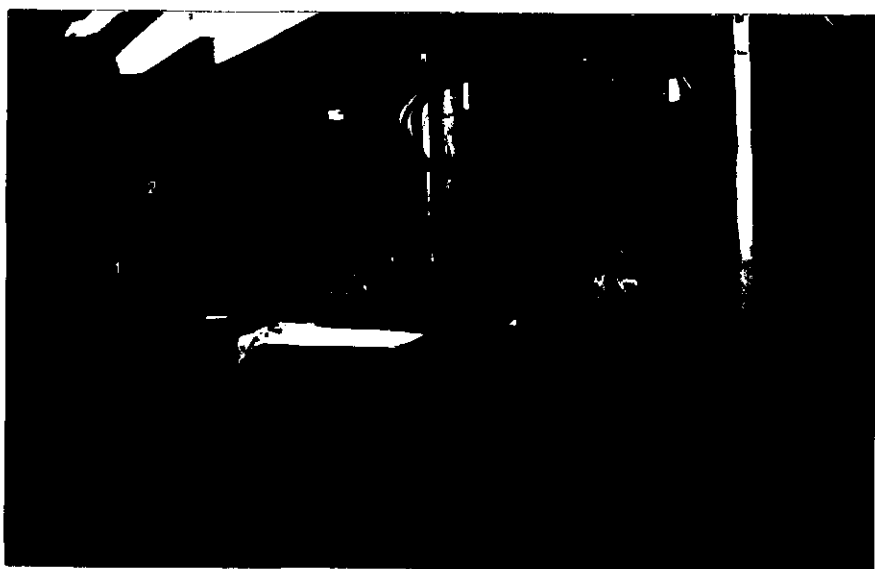
Meteorological data are measured 1.5 m above ground level at a distance of ± 20 m away from the obstacle. Parameters measured are:

a. wind speed	(m.s^{-1})
b. wind direction	$(^\circ)$
c. air temperature	$(^\circ\text{C})$
d. relative humidity	
e. precipitation	(mm)
f. global irradiance	(W.m^{-2})
g. net-irradiance at the surrounding terrain	(W.m^{-2})
	[a mixture of heather, grass and soil]



A view at the experimental site in westward direction.

1. Platform with 'HDS' and 'ELSCA'
2. Obstacle
3. Weather station



Interior of the obstacle

1. N_2 -supply
2. Air supply

} for net-radiometer

figure 4.4.

Atmospheric turbulence is determined from wind speed fluctuation measurements in three directions (i.e. u, v, w); this measurement is carried out by the agricultural University of Wageningen as a part of a forthcoming experiment; unfortunately their equipment was not yet operational during this summer. If necessary more meteorological data (cloud cover, cloud type) were gathered from synoptical stations of the airfields '*Volkel*' and '*Eindhoven*', these are located at about 15 km and 30 km respectively.

4.2 INSTRUMENTATION

4.2.1 Measurement of short- and longwave sky-irradiance

To determine the irradiance on a horizontal- and a vertical surface, the sky-radiance is measured as a function of azimuth- and elevation angle with a device called 'HDS' [34]. The device consists of a scanning head, a control- and registration unit (fig. 4.5). The scanning head has a constant speed of 12.5° per second. The way the head moves is programmable by means of a 'PROM' (*programmable read only memory*), meaning that the memory can be cleared and be programmed again. The one used is an integrated circuit which has 256 (intel 2704) programmable (8 bits) addresses.

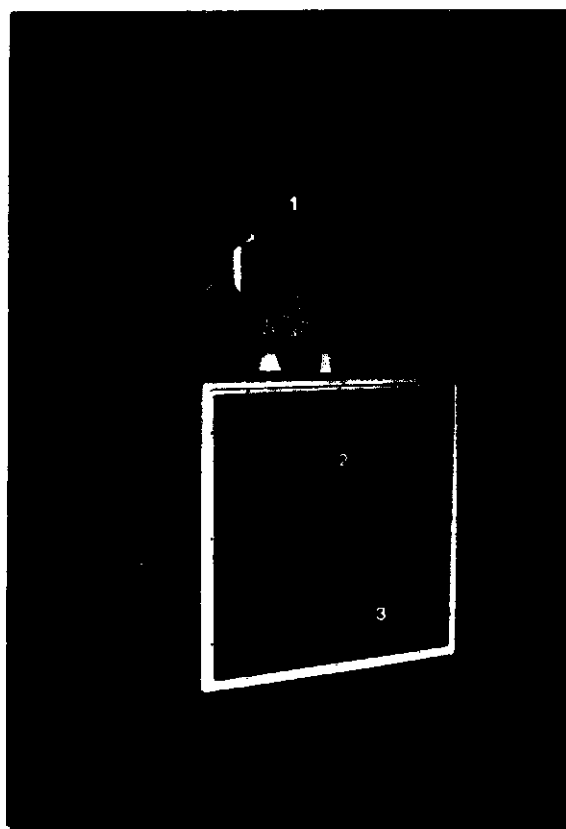
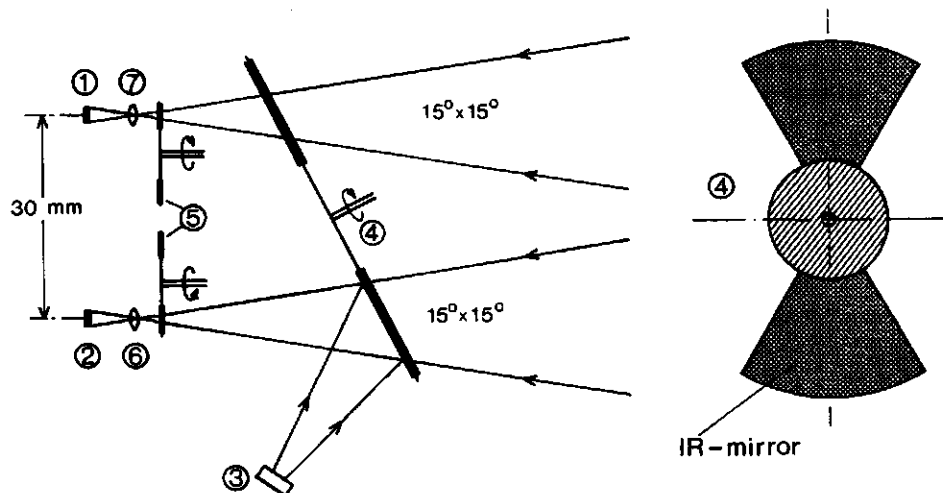


figure 4.5. Radiance distribution scanner 'HDS'.

The head consists of two detectors (fig. 4.6), one operating in $0.4-1.1 \mu\text{m}$ and one in the region $0.3-100 \mu\text{m}$. In this report the region $0.3 \leq \mu \leq 3.0 \mu\text{m}$ will be called *shortwave* region while the region $3 < \mu \leq 50 \mu\text{m}$ will be called *longwave* or *infrared* region.

The detectors used in this system are:

- a. silicium (Si) detector (Siemens BPY-12); the relative spectral responsivity is given in fig. 4.7.
- b. pyroelectric detector (Molelectron PI-71); the relative spectral responsivity is given in fig. 4.7.



1. silicium detector
2. pyroelectric detector
3. reference source (black body at $T_b = 323 \text{ K}$)
4. chopper
5. filterwheel
6. germanium lens
7. quartz lens

figure 4.6. Schematic view of the 'HDS'-sensing head.

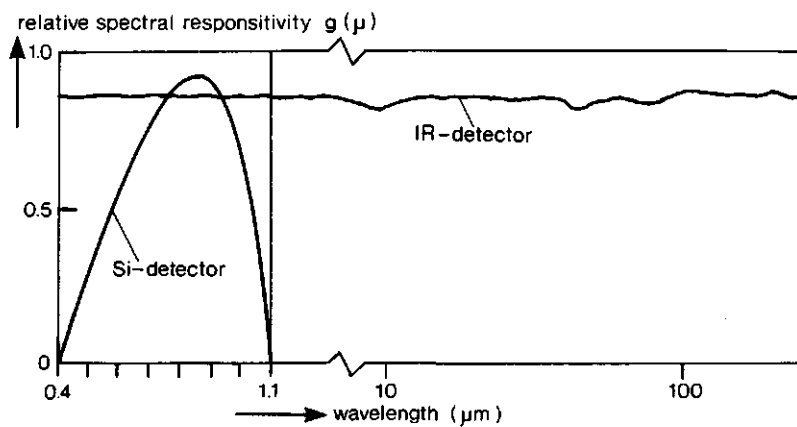


figure 4.7. Spectral responsivity of the silicium- and the IR- (pyroelectric) detector.

In front of each detector a filterwheel is mounted giving space to four filters.

The filters used in the first experiments are:

	shortwave	longwave
1.	no filter	no filter
2.	Kodak 89B (fig. 4.8)	germanium (fig. 4.9)
3.	no filter	no filter
4.	Kodak 89B	8-13 μm (block filter)

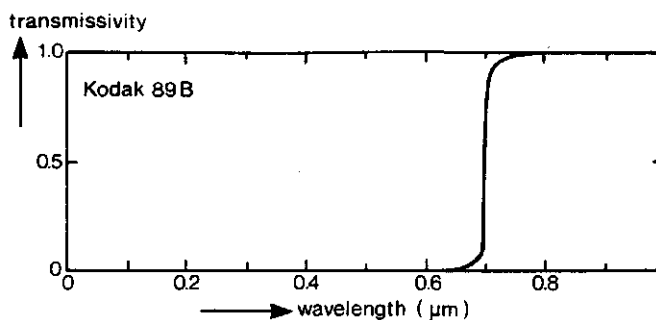


figure 4.8. Spectral transmissivity of the Kodak filter 89B.

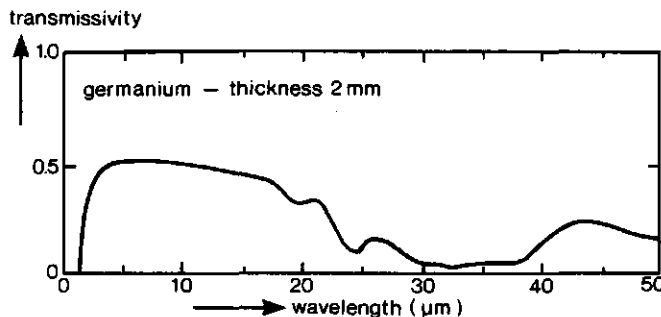


figure 4.9. Spectral transmissivity of the germanium filter

In front of both detectors there is a chopper which has a multi-function:

- a. creating an AC-signal, which is electronically much more easy to handle than a DC-signal
- b. to project a reference source (IR-part only) on to the detector
- c. uncoupling of the DC-component, which is necessary because of the high amplification used with such detectors.

The optics for both detectors is such that both have a square instantaneous field of view of $15^\circ \times 15^\circ$ (0.071 sr) and are 'looking' to the same area.

The following describes the different steps to obtain one registration (fig. 4.10, one detector).

After receiving the startpuls (0°), filter 1 of each wheel is brought into position, at the same time both detectors take 3 samples, these are integrated and stored, than the next filter is turned into position and again three samples are taken; in this way the two times four filters are measured. During the time passed the head has moved 5° ; then the whole cycle is repeated two times more, adding the new value to the stored one. Thus at the end of one measuring 'point' the total field of view covered is $15^\circ \times 30^\circ$ (0.14 sr) after the third cycle has completed data are stored on cassette-tape.

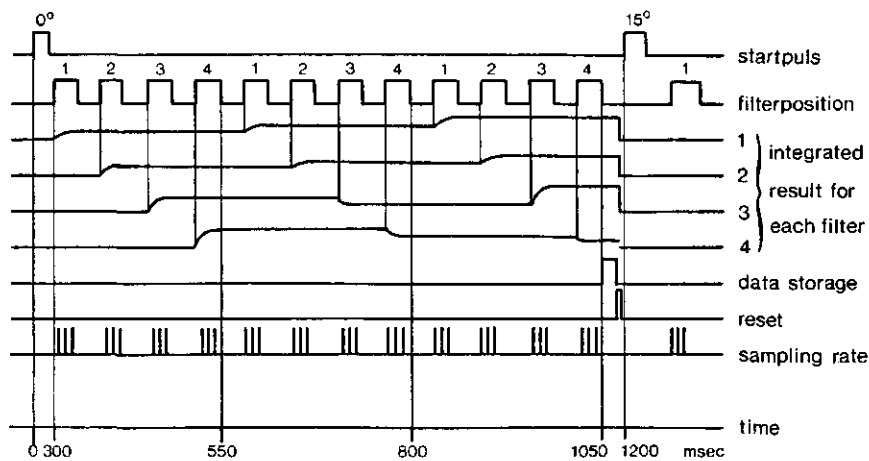


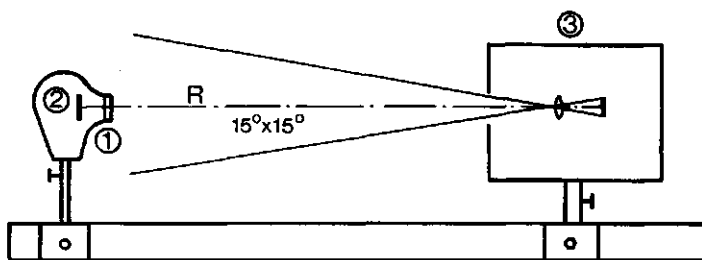
figure 4.10. Operating cycle of the 'HDS'-electronics.

A. Shortwave calibration procedure

Calibration of the Si-cel was done with a tungsten filament lamp (fig. 4.11). The lamp has known characteristics as there are:

- spectral emissivity $\varepsilon_w(\lambda)$ [37]
- transmissivity of the window τ_w
- relation between current through- and the temperature T_w of the tungsten filament.

The lamp and the complete head were placed on an optical rail and aligned carefully. The output voltage of the Si-cel was recorded for each filter as a function of the distance R between lamp and cel.



1. window (transmissivity τ_w)
2. tungsten filament
3. sensor-head

figure 4.11. Calibration set-up for the silicium detector.

The output voltage V_d is found from

$$V_d = H_s \{ S_d \} = H_s \left\{ \int_{\mu_0}^{\infty} \frac{A_w \tau_w \epsilon_w(\mu) g(\mu) f(\mu) W(\mu, T_w) d\mu}{\pi R^2} \right\} \quad (V)$$

... (4.1)

wherein:

τ_w	transmissivity of the window of the source
R	distance between the source and the entrance pupil
H_s	transfer function of cel-electronics
S_d	shortwave irradiance at the Si-cel
A_w	surface area of the tungsten filament
$g(\mu)$	relative spectral responsivity of the cel (fig. 4.7)
$f(\mu)$	spectral transmissivity of a filter
T_w	absolute temperature
$\epsilon_w(\mu)$	spectral emissivity of tungsten

(m) $(V \cdot W^{-1} \cdot m^2)$ $(W \cdot m^{-2})$ (m^2) (K)

Since the direct shortwave radiance may be about one thousand times larger than the diffuse radiance, the electronics must have a large dynamical range. This is obtained by giving the amplifier of the detector a wedge-shaped characteristic (fig. 4.12).

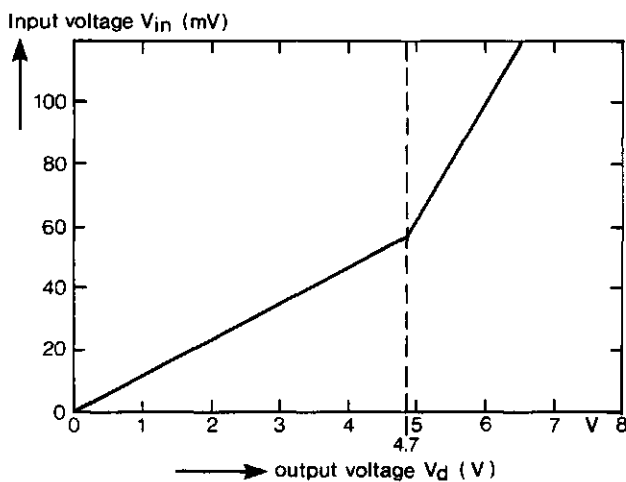


figure 4.12. Pre amplifier characteristic of the silicon detector.

H_s is determined by calibration of equation 4.1 with the arrangement of figure 4.11. If the 'HDS' is pointed to an arbitrary point in the sky a voltage V_d will be the result. This voltage is converted to the irradiance at the detector S_d by the use of H_s . Next step is to find the radiance at the entrance pupil M_p . If it is assumed that S_d is produced by a black body ($\epsilon_s = 1$) with an unknown temperature T_x , located in front of the aperture and completely filling the field of view (fig. 4.13), then M_p and S_d are given by

$$M_p = a \int_{\mu_0}^{\infty} \frac{W(\mu, T_x) d\mu}{\Omega} \quad (W \cdot m^{-2} \cdot sr^{-1}) \quad (4.2)$$

wherein Ω solid angle (0.14 sr)
 a a constant determining the source strength

and

$$S_d = V_d H_s^{-1} = a \int_{\mu_0}^{\mu} g(\mu) f(\mu) W(\mu, T_x) d\mu \quad (\text{W.m}^{-2}) \quad (4.3)$$

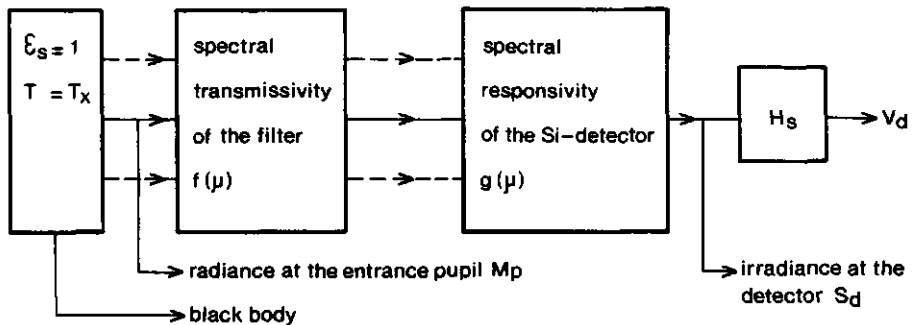


figure 4.13. Conversion of the irradiance at the detector S_d to the radiance at the entrance pupil M_p .

Solving M_p using equations 4.2 and 4.3 leads to

$$M_p = \frac{S_d}{\Omega} \frac{\int_{\mu_0}^{\mu} W(\mu, T_x) d\mu}{\int_{\mu_0}^{\mu} g(\mu) f(\mu) W(\mu, T_x) d\mu} = \frac{S_d}{\Omega \overline{g f} T_x} \quad (\text{W.m}^{-2} \cdot \text{sr}^{-1})$$

wherein $(\bar{gf})_{T_x}$ a weighted mean value in the spectral region μ_0

The temperature T_x may be found from a measurement in two different wavelength bands (determined by the spectral transmissivity of the filters f_1 and f_2) and forming the ratio:

$$\frac{s_{d,1}}{s_{d,2}} = \frac{\int_{\mu=0.4}^{1.1} g(\mu) f_1(\mu) W(\mu, T_x) d\mu}{\int_{\mu=0.4}^{1.1} g(\mu) f_2(\mu) W(\mu, T_x) d\mu} \quad (4.4)$$

Equation 4.4 has a unique solution for T_x .
This procedure is carried out for each filter.

B. Longwave calibration procedure

The IR-detector is calibrated along the same lines as described for the Si-detector. The sensor head is placed in front of a black body ($\epsilon_s = 1$) at temperature T_{bs} (the black body completely fills the field of view).

After every sample the zero level of the IR-electronics is adjusted by a reference-source ($\epsilon_s = 1$) (using the IR-mirror on the chopper blade, fig. 4.6) held at a constant temperature $T_b = 323$ K.

The output voltage V_d is determined by

$$V_d = H_\ell \{L_d\} = H_\ell \int_{\mu_0} W(\mu, T_{bs}) g(\mu) f(\mu) d\mu \quad (V) \quad (4.5)$$

wherein H_ℓ transfer function of the
cel-electronics $(V \cdot W^{-1} \cdot m^2)$

L_d longwave irradiance at the
IR-detector $(W \cdot m^{-2})$

H_ℓ is determined by calibration of equation 4.5.

If a black body with an unknown temperature T_x is placed in front of the aperture, completely filling the field of view, then the irradiance at the detector L_d is

$$L_d = V_d H_\ell^{-1} = \int_{\mu_0}^{\mu} W(\mu, T_x) g(\mu) f(\mu) d\mu \quad (W \cdot m^{-2}) \quad (4.6)$$

Equation 4.6 has a unique solution for T_x .

The radiance K_p at the aperture then is found from

$$K_p = \frac{L_d}{\Omega} \frac{\int_{\mu_0}^{\mu} W(\mu, T_x) d\mu}{\int_{\mu_0}^{\mu} W(\mu, T_x) g(\mu) f(\mu) d\mu} = \frac{L_d}{\Omega} \frac{1}{(\overline{gf}) T_x} \quad (W \cdot m^{-2} \cdot sr^{-1})$$

C. Integrated results

As already stated the scan pattern of the head is programmable and therefore there are many possible ways to scan the upper hemisphere.

Since the field of view is fixed, there is an increasing overlap between (neighbouring) elements with increasing elevation angle.

The start of the scan is in horizontal direction at an elevation of 7.5° (fig. 4.14); after completion of the circle the head is elevated 15° and the next scan circle is made in reverse direction. In total 6 circles are needed to cover the entire surface of the hemisphere.

To minimize overlap (at most by two neighbouring elements), the scan angle in horizontal direction is enlarged ($\Delta\phi$) with increasing elevation angle (fig. 4.15).

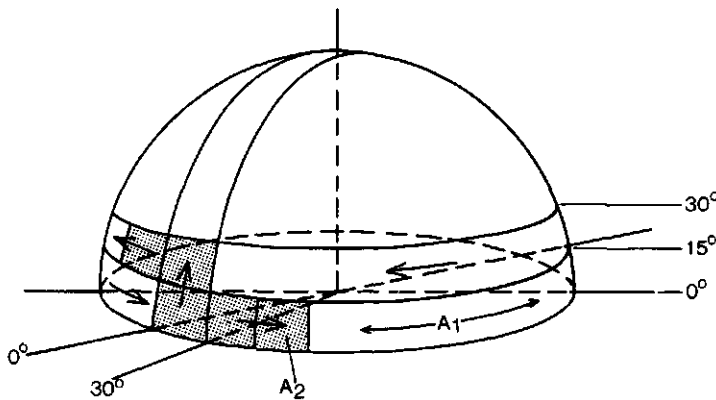


figure 4.14. Scan pattern of the 'HDS'.

ψ	ϕ	345	15	45	75	105	135	165	195	225	255	285	315	ψ	$\Delta\phi$	η	N
ψ		15	45	75	105	135	165	195	225	255	285	315	345				
75-90														72	0.69	5	
60-75														45	0.43	8	
45-60														36	0.27	10	
30-45														30	0.21	12	
15-30														30	0.08	12	
0-15														30	0.01	12	

(ψ, ϕ) elevation- resp. azimuth angle in °

$\Delta\phi$ azimuth increment in °

η overlap

N number of elements at a given elevation angle

figure 4.15. Schematic view of all scan elements, including the overlap η and including the number of elements N per elevation angle.

In this way a total time of nearly 3 minutes is needed to complete a scan of the entire hemisphere.

A total of 59 elements is formed, the overlap η depending on elevation ψ of the element.

The overlap is determined from the ratio of the real surface of the scan-circle A_1 on the sphere and the total area occupied by the number of 'HDS'-elements N on that circle i.e. $N \times A_2$ (fig. 4.14):

$$\eta = 1 - \frac{A_1}{A_2} = 1 - \frac{2\pi(\sin \psi_2 - \sin \psi_1)}{N \left(\frac{\pi}{6} \times \frac{\pi}{12} \right)}$$

wherein ψ_1 and ψ_2 are the upper- resp. lower boundary elevation angle of the circle

After correcting each element $Q(i,j)$ for the overlap, the irradiance at a horizontal- (Q^h) and at a vertical (Q^v) plane is found from ($Q(i,j) = M_p(i,j)$ or $K_p(i,j)$ for short- resp. longwave radiation):

a. horizontal plane

$$Q^h = \sum_{i=1}^6 \sum_{j=1}^N Q(i,j) \sin \psi_i \quad (\text{W.m}^{-2})$$

b. vertical plane

$$Q^v = \sum_{i=1}^6 \sum_{j=1}^N Q(i,j) \cos \psi_i \cos(\varphi_j - \varphi_o) \quad (\text{W.m}^{-2})$$

with $Q^v = 0$ for $\cos(\varphi_j - \varphi_o) \leq 0$

wherein φ_o orientation of the vertical surface with respect to the north

(north: $\varphi_o = 0$ and east: $\varphi_o = \frac{\pi}{2}$)

To be able to compare the results with other measurements like a solarimeter, the irradiance Q^h in the spectral region $0.4-1.1 \mu\text{m}$ is transformed to the irradiance Q_g in the spectral region of $0.3-3 \mu\text{m}$ (global irradiance).

This is done by transforming the radiance within each element, knowing its temperature T_x and the transmission characteristics of the glass sphere τ_g of the solarimeter (Kipp & Zonen, fig. 4.16).

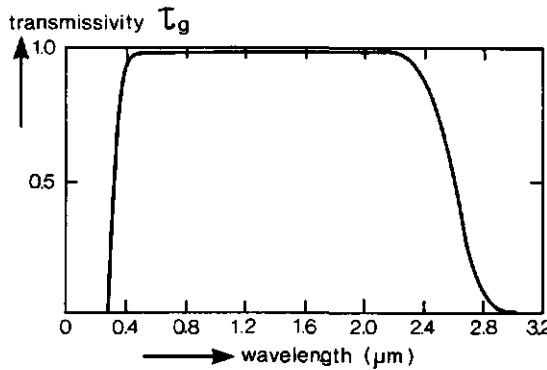


figure 4.16. Spectral transmissivity of the glass dome of a Kipp solarimeter.

If it is assumed that there is no difference in atmospheric transmissivity in both regions, the irradiance then is found from

$$Q_g = a \int_{\mu=0.3}^{3.0} W(\mu, T_x) \tau_g(\mu) d\mu \quad (\text{W.m}^{-2})$$

where a is determined by

$$Q^h = a \int_{\mu=0.4}^{1.1} W(\mu, T_x) d\mu \quad (W.m^{-2})$$

The irradiance at a vertical plane is found the same way as described before.

Figure 4.17 shows the 'HDS' positioned on the platform (right one), the left one is the 'ELSCA' which will be dealt with in section 4.2.4.



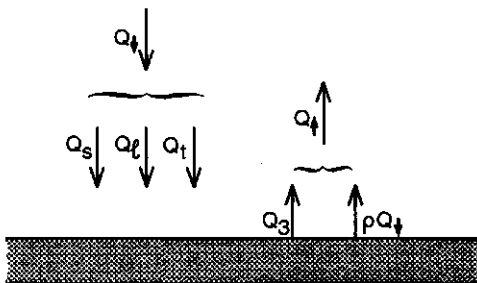
figure 4.17. Location of the 'ELSCA' (left) and 'HDS' (right) on the platform.

4.2.2 Net-radiometer

The net-radiation Q_N incident on a surface is given by (fig. 4.18)

$$Q_N = Q\uparrow - Q\downarrow \quad (W \cdot m^{-2})$$

wherein $Q\uparrow$ and $Q\downarrow$ are the incoming and outgoing radiative components respectively.



- $Q\uparrow$ upward radiation
- $Q\downarrow$ downward radiation
- Q_s shortwave radiation
- Q_ℓ longwave radiation
- Q_t incident radiation due to the surrounding terrain
(non horizontal surfaces only)
- Q_3 emitted radiation
- $\rho Q\downarrow$ reflected downward radiation

figure 4.18

The net-radiation is measured with a net-radiometer (Middleton instruments); it is generally assumed that the responsivity is independent of wavelength. The instrument essentially consists of a sensing element

surrounded by inflatable polythene wind shields (fig. 4.19 and 4.20). The sensor is a flat thermopile where the 'hot'- and 'cold' junctions are formed by the front- and backside of the sensing element (coated black). Placed above a surface this instrument therefore directly measures the net-radiation (i.e. temperature difference across the sensing element).

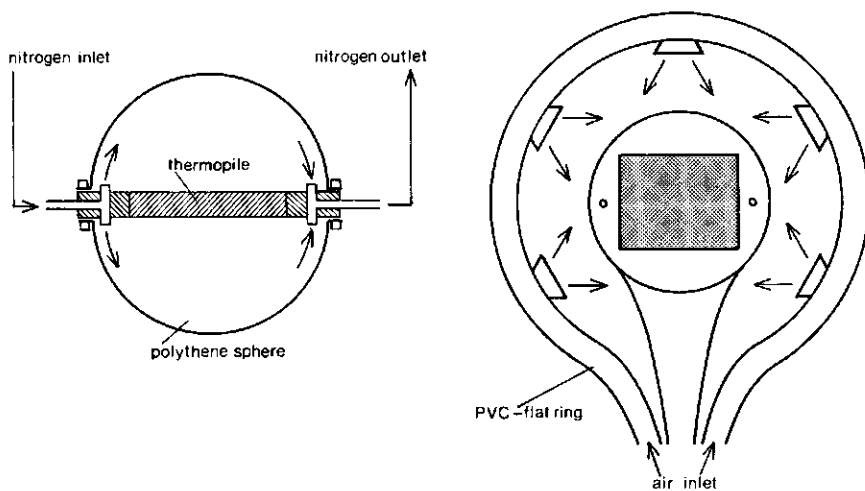


figure 4.19. Schematic view of a net-radiometer.

The advantage of polythene is the very good transmissivity over a broad wavelength interval, the disadvantage however is its porosity for water vapour. To prevent diffusion of water vapour into the spheres (and damaging the thermopile), these are continuously washed with dry nitrogen, keeping the pressure slightly higher than ambient atmospheric pressure.

Furthermore the spherical shape of the (very thin) polythene is maintained by this overpressure.

Through an extra ring, surrounding the sensor (fig. 4.19 and 4.20) air is blowing over the spheres, to prevent condensation

on the polythene and to keep them on air temperature [42]. Air is supplied by a fan ($5 \text{ m}^3/\text{min}$) placed inside the obstacle. The device (without air-ring) is supplied with a calibration certificate (typical $0.40 \text{ mV} \cdot \text{mW}^{-1} \cdot \text{cm}^{-2}$). The sensors are used in a horizontal- as well as in a vertical position at about 40 cm away from the surface (fig. 4.20).

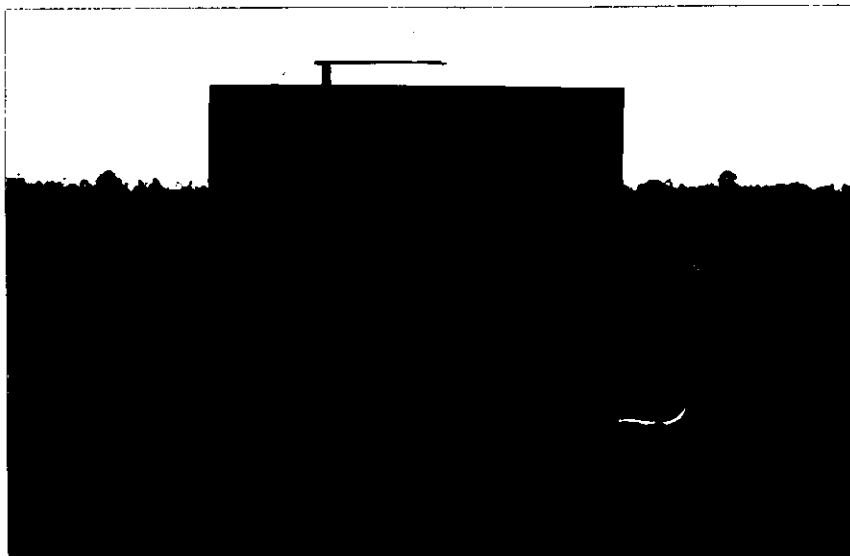


figure 4.20. Location of the net-radiometers.

The most critical feature of this sensor is the change of the transmissivity of the polythene in the open field (rain, dirt). Depending on the type of weather, cleaning of the spheres is necessary once or twice a week; but after a certain time depending on the season [42] the transmissivity is degrading seriously and therefore the spheres have to be exchanged. For comparison the transmissivity of a new-, (starting in January 1981) three months- and 6 months old sphere is given in figure 4.21.

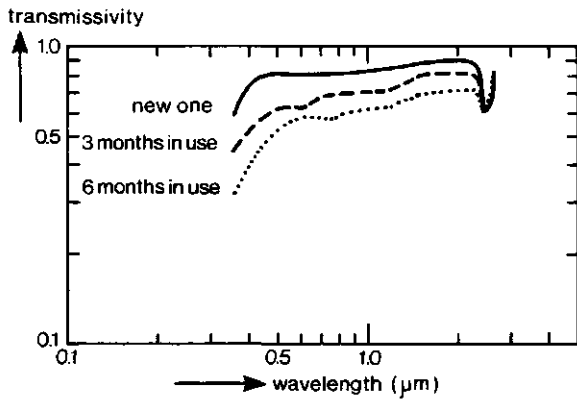


figure 4.21. Spectral transmissivity of a polythene sphere of a net-radiometer related to atmospheric and environmental influences.

4.2.3 Heat flow sensor

The measurement is based on the principle that a temperature difference ΔT across a thin uniform layer is proportional to the heat flow through that layer Q_6 (eq. 1.3) as,

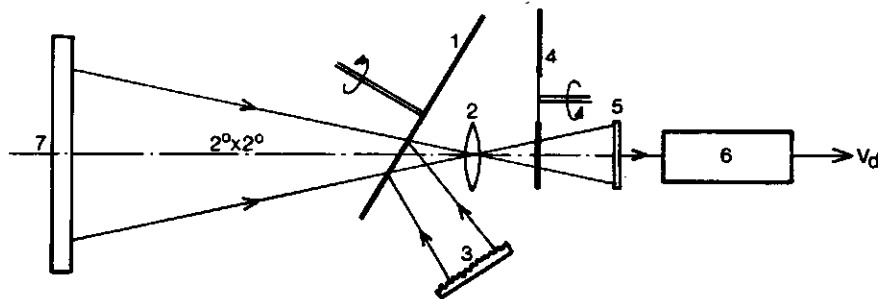
$$Q_6 = - \frac{\lambda}{d} \Delta T \quad (\text{W.m}^{-2})$$

where λ thermal conductivity of the layer ($\text{W.m}^{-1}.\text{K}^{-1}$)
 d thickness of the layer (m)

The TPD ('Technisch Physische Dienst') in Delft, produces heat flow sensors of different sensitivities and shapes. The one used in this experiment has the shape of a disk (WS 32 diameter 50 mm, thickness 3 mm) with thermal characteristics close to those of polyvinylchloride (PVC). The sensors are supplied with a calibration certificate (typical $10-20 \text{ W.m}^{-2}.\text{mV}^{-1}$).

4.2.4 Scanning radiometer 'ELSCA'

This device [19] is constructed the same way as the 'HDS' i.e. a scanning head, a control unit and a registration unit. Figure 4.22 shows the interior of the scanning head. Analogous to the 'HDS' (IR-part), the radiation is chopped and then passes a lens, a filter and eventually reaches the detector. The detector is of the pyroelectric type (Molelectron P1-71, fig. 4.7) and together with the optics used giving the sensor an instantaneous field of view of $2^\circ \times 2^\circ$ (this is the main difference with the 'HDS').



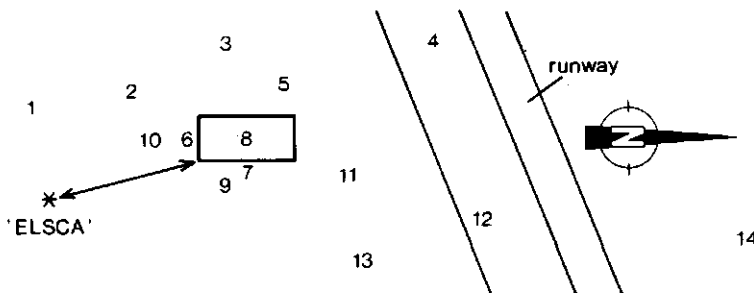
1. chopper (right part of fig. 4.6)
2. IR-lens
3. reference source
4. filterwheel (4 filters)
5. detector
6. electronics
7. black body for calibration purposes

figure 4.22. Schematic view of the sensing head of the 'ELSCA'.

Again 4 filters are used

1. germanium (fig. 4.9)
2. 3.5-5.1 μm
3. 8.2-13.9 μm
4. 8.8-10.8 μm

Located at an elevated position (± 7 m) the device scans the obstacle and direct surroundings, giving the radiative temperature θ_s (fig. 4.23, the features given may be meaningless when not used in connection with this experiment).



1. 'brown' heather
2. 'dark' soil
3. 'sparse' grass in heather
4. 'grass' adjacent to runway
5. 'heather'
6. southside of the obstacle
7. east side of the obstacle
8. top surface
9. 'soil' close to the obstacle
10. 'soil'
11. 'heather'
12. 'grass' adjacent to runway
13. 'sparse grass in heather'
14. 'tree line' at ± 1 km

figure 4.23. Scan pattern of the 'ELSCA'

Each position of the head is stored in memory ('PROM'); up to a maximum of 256 positions can be stored.

Having arrived at a certain position the head stops and a measuring cycle (4 filters) is started (fig. 4.10).

Using a black body with known temperature T_{bs} , completely

filling the field of view, then the output voltage of the detector V_d is

$$V_d = H_\ell \{L_d\} = H_\ell \int_{\mu_0}^{\mu} W(\mu, T_{bs}) g(\mu) f(\mu) d\mu \quad (V) \quad (4.7)$$

H_ℓ is calibrated with eq. 4.7 using different temperatures T_{bs} . If a black body with an unknown temperature T_x is used, the irradiance at the detector L_d is

$$L_d = V_d H_\ell^{-1} = \int_{\mu_0}^{\mu} W(\mu, T_x) g(\mu) f(\mu) d\mu \quad (W \cdot m^{-2}) \quad (4.8)$$

Equation 4.8 has a unique solution for T_x .

The radiance at the entrance pupil K_p then is found from

$$K_p = \frac{L_d \int_{\mu_0}^{\mu} W(\mu, T_x) d\mu}{\Omega \int_{\mu_0}^{\mu} g(\mu) f(\mu) W(\mu, T_x) d\mu} = \frac{L_d}{\Omega} \frac{1}{(\bar{g}f)_{T_x}} \quad (W \cdot m^{-2} \cdot sr^{-1})$$

This procedure is carried out for each filter.

As already mentioned, in practice often the radiative temperature θ_s is used, solved from

$$K_p = \frac{1}{\pi} \int_{\mu_0}^{\mu} W(\mu, \theta_s) d\mu$$

4.2.5 Infrared reflectometer

To make a distinction (optically) between two objects it is necessary that a difference exists between the irradiance received from both objects. In the infrared such a difference may be caused by a difference in emissivity and/or a difference in temperature (cf. section 3.7).

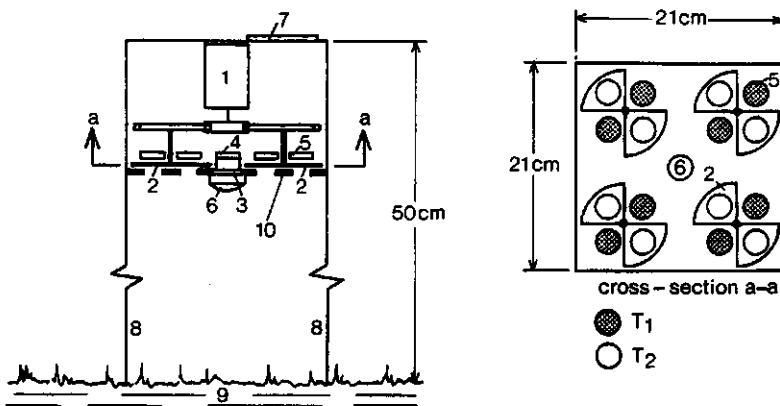
For a solid material it is relatively easy to measure the temperature, this in contrast to that of a loose material. A simple way to determine emissivities (only solid materials) is to heat the sample and to measure both the radiative- and real temperature θ_s resp. T_s . The emissivity ϵ_s is then found from (neglecting reflected radiation):

$$\epsilon_s = \left(\frac{\theta_s}{T_s} \right)^4$$

For loose materials and vegetation this method is not applicable, therefore an instrument has been developed to overcome this problem [38]. With this device in fact the (IR) reflectivity ρ_ℓ of a surface is determined from which ϵ_s is found as (Kirchhoff's law)

$$\epsilon_s = 1 - \rho_\ell$$

The construction is shown in figure 4.24; the sample-surface is irradiated alternately by two black bodies (at different temperatures T_1 and T_2). As shown in the figure the top of the instrument consists of a total of 16 black bodies and a detector (thermopile) located in the centre. At one instant all sources at T_1 are screened by the chopper blade (chopper frequency is 2 cycles) on this moment the top surface radiates as a black body at temperature T_2 .



1. chopper motor	6. 'fish-eye' lens
2. chopper blade	7. display
3. filter	8. IR-mirror
4. detector	9. sample surface
5. black bodies ($T_1 > T_2$)	10. support

figure 4.24. Construction of the IR-reflectometer.

Due to the mirrors the sample is irradiated from all directions; the reflected radiation irradiates on its turn the top surface where the detector is located. To enhance the sensitivity for small angles a 'fish-eye' lens is placed in front of the detector.

Since the sample is irradiated diffusely the quantity measured is the diffuse reflectivity ρ_ℓ (different spectral filters can be used). From both readings the reflectivity is found from

$$\rho_\ell = \int_{\mu_0}^{\infty} \left\{ W(\mu, T_1) - W(\mu, T_2) \right\} f(\mu) d\mu = a(V_{d_1} - V_{d_2})$$

where V_d detector output voltage (V)

The constant a is determined by using an IR-mirror as sample ($\rho_f = 1$); a is determined for each filter used later on. The result of a measurement is directly displayed.

Figure 4.25 shows the device as it stands (right hand side) and also shows the black bodies and detector assembly (left hand side).

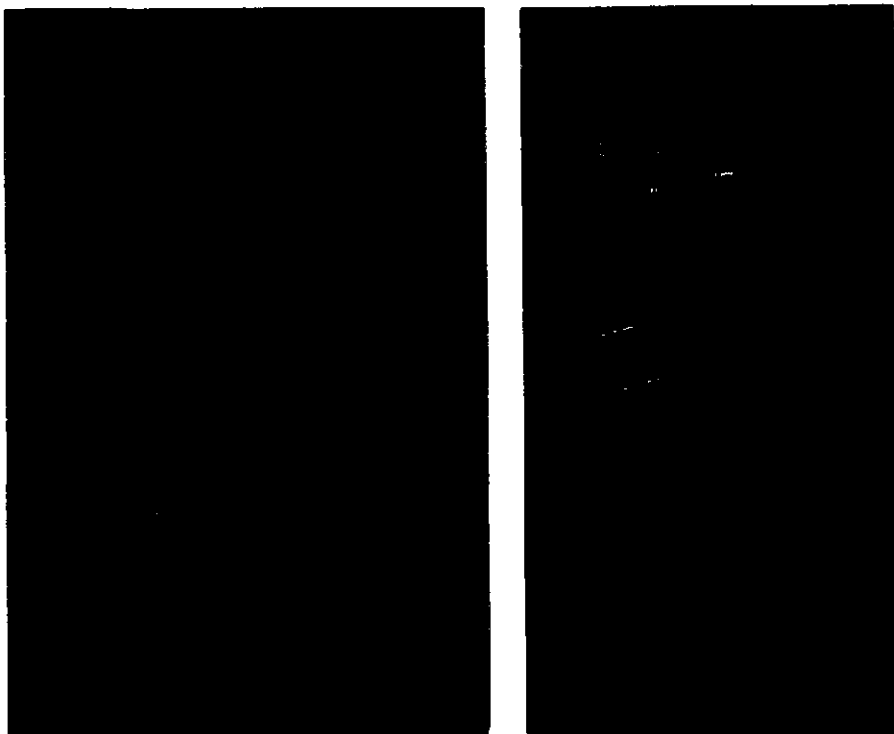


figure 4.25. IR-reflectometer, left part showing the black bodies and detector assembly, the right part shows the device as it stands.

4.2.6 Meteorological measurements

A small weather station [35] is located in the NE corner of the experimental site (fig. 4.4 and 4.26). Parameters are measured 1.50 m above ground level; these are

1. *Wind speed and wind direction*

Both measurements are combined in one device.

Manufacturer: Thiess (type 4.3320).

2. *Air temperature*

This temperature is determined by a nickel resistor (NI-1000, from Wallac Oy) mounted in a radiation shield and positioned in a weather-box (Thiess, type 1.2175.03). This box is ventilated with a small fan (Pabst, type 2050) which is mounted in a vertical wall and sucks out the air of the box and thereby passing the thermometer.

3. *Relative humidity*

This parameter is determined by a hair hygrometer (Thiess, type 1000).

This sensor is also located in the weather-box.

4. *Precipitation*

The amount of rain is measured by a sensor developed by TNO. The most characteristic feature of this sensor is the creation of small droplets of about the same size. The number of droplets is counted and is a measure of the amount of water fallen into the pan.

5. *Shortwave irradiance at a horizontal plane (global irradiance)*

This parameter is measured with an albedometer (Kipp, type CM7) also called solarimeter.

6. *Net-radiation*

This parameter is measured with a net-radiometer.

It is placed above the ground (a mixture of heather, grass and soil).

Manufacturer: Middleton instruments.

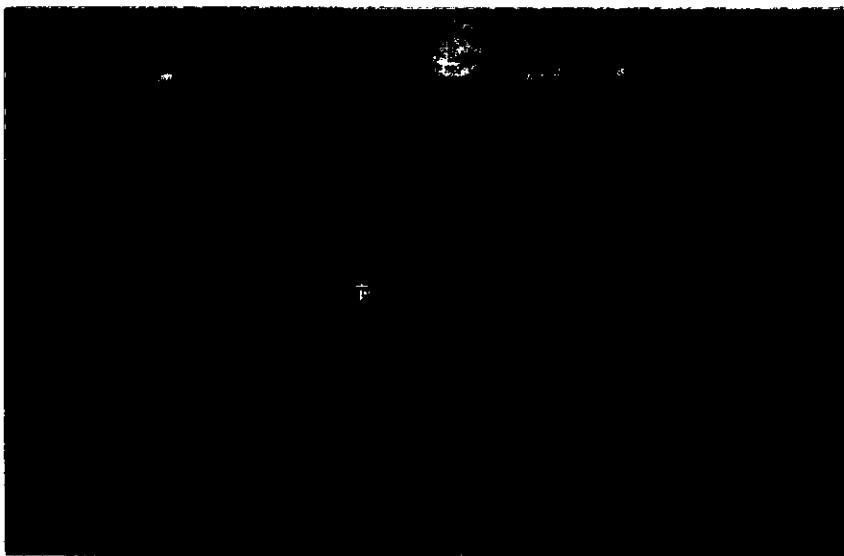


figure 4.26. View on the weather station taken from the platform in NE-direction.

4.3 DATA ACQUISITION

Systems as 'HDS' and 'ELSCA' are selfregistering units. The built-in electronics drives a cassette-recorder. Total capacity of a cassette-tape is about 45000 eight bits words. In practice this means that with a repetition time of 10 minutes (having 15 measuring points) the 'ELSCA' can record for the duration of 120 hours and the 'HDS' for about 25 hours, both using 4 filters. Both devices measure instantaneous values (in time and position) i.e. 'point' measurements without integration.

The weather station makes use of the same kind of recorder; in this case however integration of the signals takes place over a given (adjustable) time interval, in our case 5 minutes. All other sensors (thermocouples, heat flow- and net-radiation sensors) are read out through a multiplexer, controlled by a microprocessor. The 64 channel multiplexer scans all input channels in about 6 seconds, the values are digitized and stored in memory; the next reading is added and this sequence is repeated until a given (integration) time (10 minutes) has elapsed. Finally the results are written to cassette-tape. All the 'cold' junctions of the thermocouples are joined together and are in good thermal contact with a large copper-block. The temperature of this block is measured with a resistor (P_t , 100 Ω). The temperature readings are calibrated with this reference temperature.

4.4 INFRARED IMAGERS

Aerial imagery was scheduled to be taken at certain time points during the late summer of 1981 by:

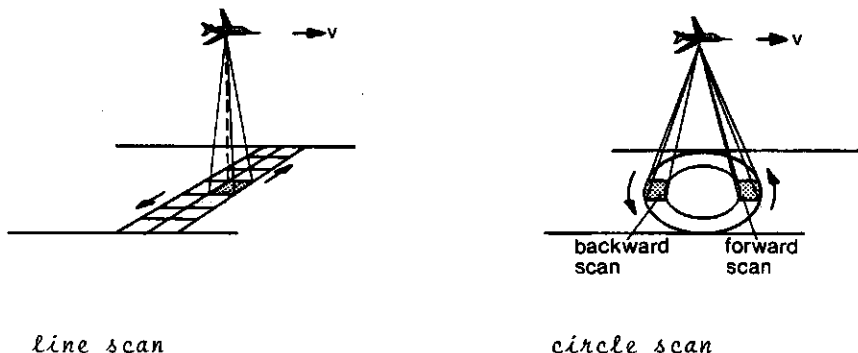
- a. The 306 reconnaissance squadron of the Royal Dutch Airforce based at the airbase Volkel.

An 'IRLS' (Infrared Line Scanner) operational in 8-14 μm which is called 'ORPHEUS', is available. Collected information is saved on film negative.

- b. The International Training Centre (ITC) located at Enschede. For educational work the ITC has a small airplane available (a Piper Navajo). In cooperation with TNO, flights can be made using two different IR-scanners called 'FLORIS'- and 'CIRCLE' scanner.

The 'FLORIS' is a line scanner [29] while, as the name already suggests the 'CIRCLE' scanner has a circular scan pattern [30].

Figure 4.27 shows the scanning principle of both scanners.



line scan

circle scan

figure 4.27. Scan pattern used by a line scanner (left part) and a circle scanner (right part).

Table I shows some characteristics of both scanners.

The geometrical resolution on the ground depends on the flight speed v and -height h .

To get joining scan lines on the ground the following equation must be obeyed.

$$\omega \times p = v \quad (\text{m.s}^{-1}) \quad (4.9)$$

where ω angular speed of the scan mirror (r.s^{-1})
 p resolution element on the ground (m)
 v flight speed (m.s^{-1})

feature	'FLORIS'	'CIRCLE'
Field of view ($^{\circ}$)	120	90
instantaneous field of view (mrad)	2	5 x 7
spectral interval (μm)	3-5 and 8-14	8-14
minimum resolvable temperature (K)	0.1	0.01

Table I. Some characteristics of the 'FLORIS'- and the 'CIRCLE' scanner.

As can be seen from table I the 'FLORIS'-scanner has a high geometrical resolution while the 'CIRCLE'-scanner has a high temperature resolution.

Applying eq. 4.9 to the 'CIRCLE'-scanner with

$$\begin{aligned} \omega &= 25 & (\text{r.s}^{-1}) \\ v &= 100 & (\text{m.s}^{-1}) \end{aligned}$$

results in a geometrical resolution of: $p = 4 \text{ m.}$

Given this value of p , the flight level h is found to be about 285 m (fig. 4.28).

Collected data is saved on film negative ('ORPHEUS') and analog instrumentation tape.

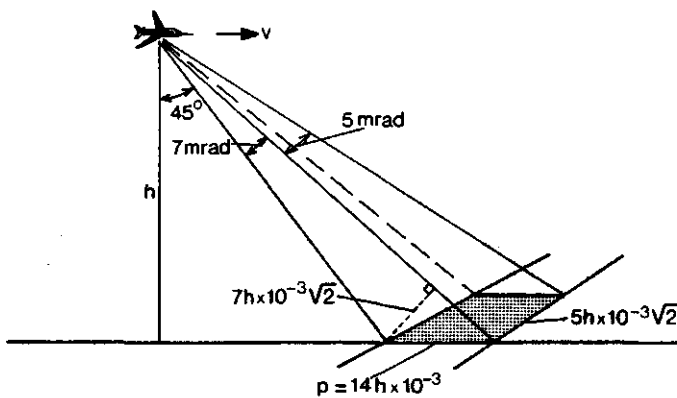


figure 4.28. Determination of the resolution element on the ground for the 'CIRCLE' scanner.

For Forward Looking InfraRed (FLIR) systems, the contrast between obstacle surfaces themselves is important. The 'CIRCLE'-scanner detects the obstacle two times, firstly during approach and secondly after having passed the obstacle (45° depression angle). During clear sunny days the contrasts are very large; during clear nights the top surface always shows a negative contrast with the vertical surfaces, due to radiative cooling of the top surface.

Figure 4.29 shows an IR-image taken by the 'FLORIS'-scanner at 13.00 GMT on 18 August (8-14 μm).

Figure 4.30 gives an overview of what is seen on the image. As outlined in section 3.6, a radiation contrast is converted to a contrast in grey level on a film negative. On a positive print an 'apparent warm' area looks white in contrast to a 'cold' area which looks more black.

The picture is taken just after the sun has broken through after a morning of overcast sky. The white (in the visible spectrum) portacabine sticks out clearly as a 'cool' black spot; the obstacle shows up a bit cooler than the mixture (fig. 4.30) the difference between the heather and cut heather is striking, obviously the cut heather is more dead than alive (evaporating mechanism is missing). The road pattern

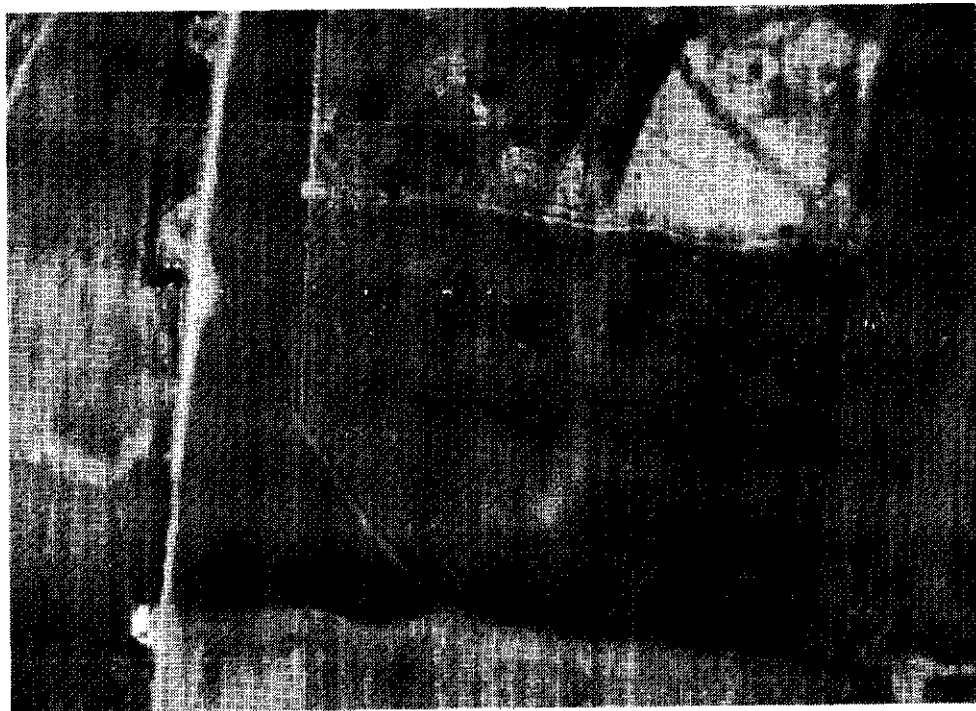


figure 4.29. IR-picture taken with the 'FLORIS' line scanner (8-14 μ m).

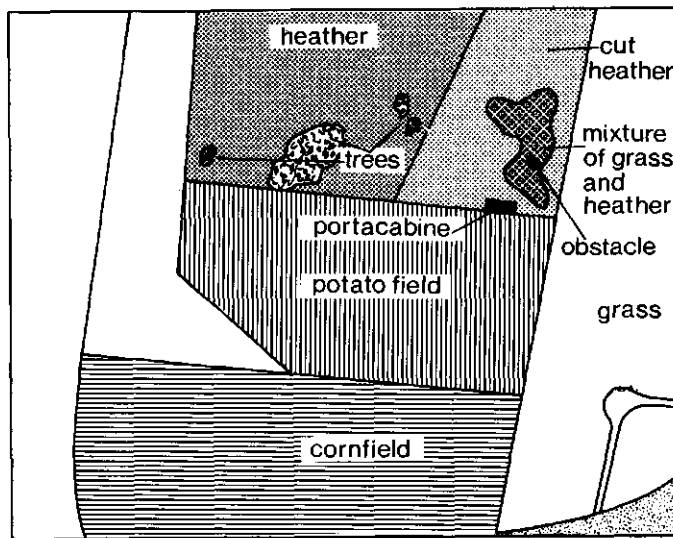


figure 4.30. Description of some features in fig. 4.29.

in the heather field in reality does not exist, but has been there in former days. Since the soil structure therefore is different, the thermal behaviour is slightly different and the roads show up in the picture. Figure 4.31 shows a picture taken with the 'CIRCLE'-scanner; the lower part shows the forward scan and the upper part the backward scan.



figure 4.31. IR-picture taken with the 'CIRCLE'-scanner (8-14 μ m).

Figure 4.32 gives an overview of what is seen on the image. On both pictures the portacabine is visible, however much more vague than in figure 4.29, due to the low geometrical resolution of this scanner; it needs a careful look to see the obstacle; there is something of a black area but without further knowledge the obstacle as such is not detectable.

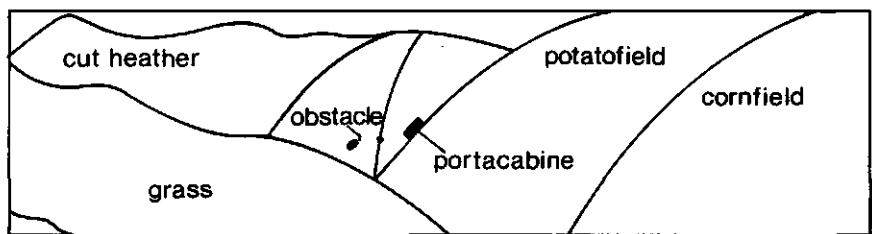
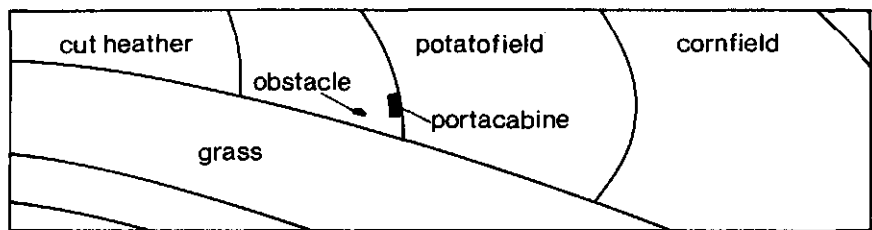


figure 4.32. Description of some features in fig. 4.31.

5.0 ANALYSIS OF DATA AND RESULTS

5.1 SUMMARY OF PERFORMED MEASUREMENTS

Having finished the basic tests and calibration procedures the equipment was stationed in the field by the end of May 1981.

Many problems were encountered during the first weeks. As for instance the registration of the thermocouples with the microprocessor/multiplexer system was correct during most times of the day but every evening from about 19.00 hours until 04.00 in the morning something went wrong. It nearly took a month to find out that this was due to atmospheric interference. It appeared that thermocouple wires served as radio antennas and since the multiplexer input gates were not in common mode the input signal was tilted randomly. The fact that this happens around 19.00 hours is caused by condensing of the so called F1 and F2 layer and thereby forming a reflectionlayer for shortwave radio frequencies. A rain detector preventing the 'HDS' from starting during a rain period broke down, so it could operate only when somebody was around or, automatically during a longer period of continuous dry weather.

Unfortunately the field trial of the Agricultural University of Wageningen was not started yet this summer, therefore atmospheric turbulence (a parameter they would have measured) is not known.

From the end of July on all the systems worked satisfactory and from that period on data are used for analyzing purposes.

5.2 SKY-RADIANCE DISTRIBUTION

5.2.1 Shortwave irradiance

In the beginning of the measuring period a 'HDS'-scan was made every hour, in order to suppress the amount of data. However, it soon appeared that the measured values were very typical for that very 'moment' caused by the fact that the sun is within the field of view for only a very short time (about 3 seconds). For instance it was observed that when cirrus clouds passed the sun, the solar radiance decreased at once, while the solarimeter did not react at all to this change. To be able to compare the 'HDS'-measurements with the solarimeter, measurements were taken at 10 minutes intervals; it is anticipated that this will give sufficient information to determine a mean value.

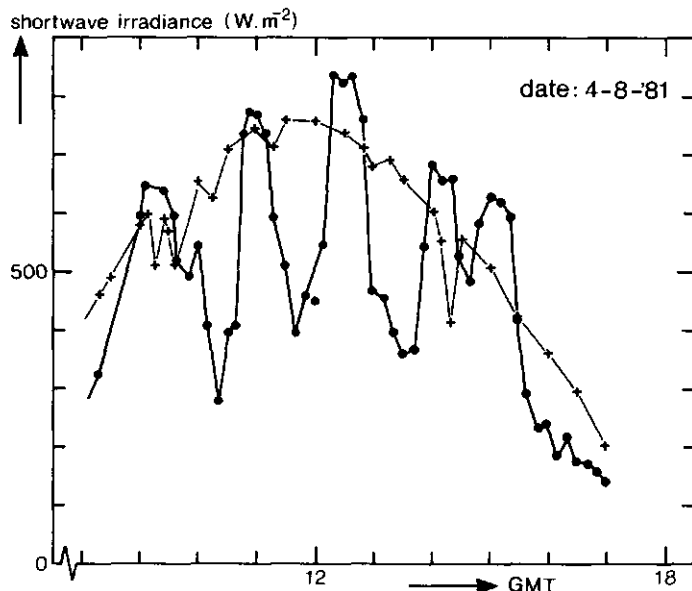
Another problem is that the radiance distribution as it is measured cannot be compared with other measurements; so, first an integration has to be performed and then the data have to be transformed to the proper wavelength-interval of the solarimeter (i.e. $0.3 \leq \lambda \leq 3 \mu\text{m}$).

From the limited amount of data available, the 4th of August 1981 has been chosen for analyzing purposes.

Some meteorological features of this day are: fog at night changing to light haze during daytime; minimum and maximum air temperature of 11 resp. 29 °C; little wind ($\leq 1 \text{ m.s}^{-1}$) from a variable direction.

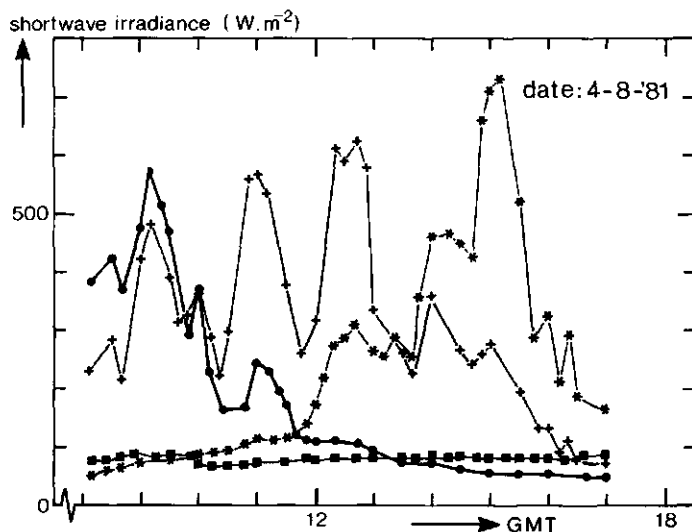
Figure 5.1 shows a comparison between the global irradiance as it is measured with a solarimeter and the shortwave irradiance at a horizontal surface determined from the sky-radiance distribution measured with the 'HDS'.

Figure 5.2 shows the shortwave irradiance at different vertical orientations, determined from the radiance distribution. The periodic behaviour of the 'HDS'-readings is striking. A more close look shows that this periodicity disappears when the sun is not within the field of view, suggesting that the sun is the cause of this behaviour.



- solarimeter reading (global irradiance)
- shortwave irradiance at a horizontal plane using the 'HDS'

figure 5.1. Shortwave irradiance at a horizontal plane.



shortwave irradiance at a vertical plane using 'HDS'-values with the orientation:

- north
- south
- east
- * west

figure 5.2. Shortwave irradiance at a vertical plane.

To analyse this, the solar elevation- and azimuth angle are determined (section 3.1) and are given in figure 5.3.

Furthermore the relative spatial responsivity of the Si-detector is given in figure 5.4.

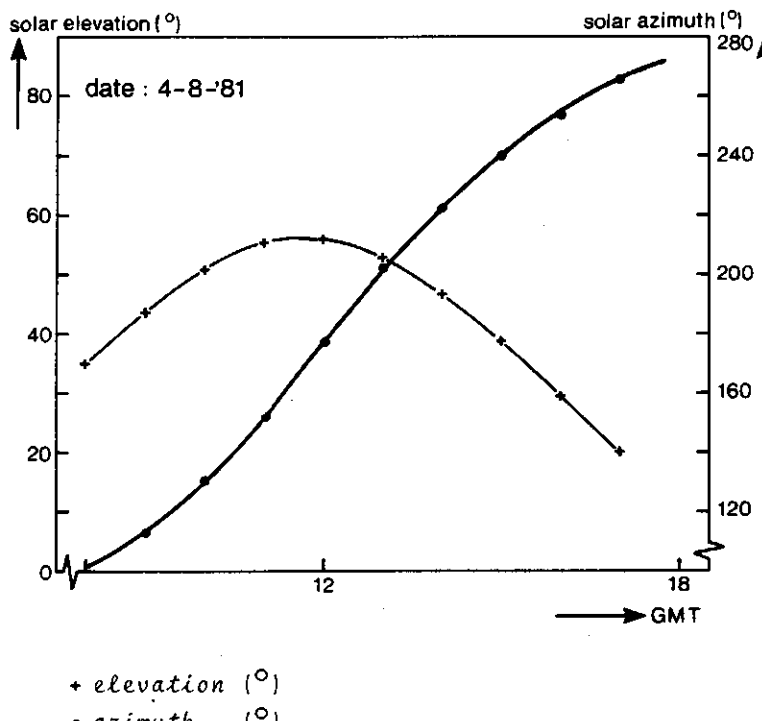


figure 5.3. Solar bearing as a function of time.

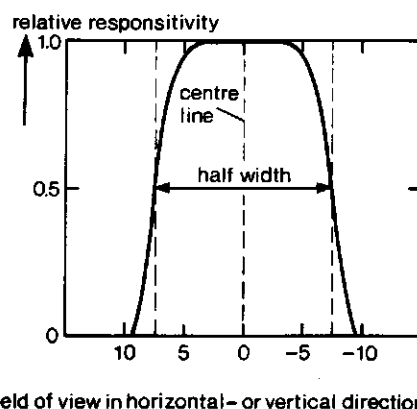


figure 5.4. Spatial responsivity of the Si-detector.

From this figure it is obvious that when the sun is not located within a few degrees from the centre, the output voltage of the detector is rapidly decreasing with increasing off-centered position. To show this effect we keep track of the sun passing through a 'HDS'-element giving by the elevation- and azimuth boundaries of resp. 45° - 60° and 135° - 165° (fig. 5.5).

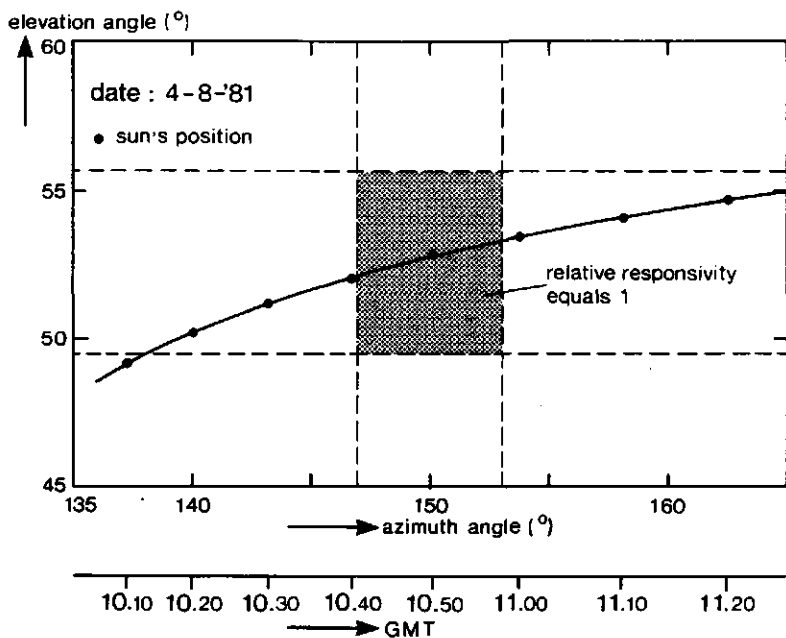


figure 5.5. Position of the sun as a function of time, relative to a fixed position of the 'HDS'.

The figure shows that, as a function of time the sun approaches the centre of the element, passes it at about 10.50 GMT and leaves the element again at about 11.20 GMT. All together it is clear that the 'HDS' cannot be used when, in general, a point source is present; the only exception to this is the case wherein the point source is located in the centre (this is also the case during calibration procedures). To meet the requirements just mentioned a time is chosen where the sun

is located near the centre and where a reasonable agreement exists between the solarimeter- and integrated 'HDS'-values i.e. 11.00 GMT.

Figure 5.6 shows the measured radiance distribution at 11.00 GMT on 4 August 1981.

date 04-08-'81			time (GMT) 11.00						spectral region $0.3 \leq \mu \leq 3 \mu\text{m}$				0° = north 90° = east		
ψ	345	15	45	75	105	135	165	195	225	255	285	315	ψ		
ψ	15	45	75	105	135	165	195	225	255	285	315	345	$\Delta\phi$		
75-90	30.5			41.8			30.5			20.6			20.6		
60-75	24.1		31.2		57.4		125.4		124.8		55.3		34.9		45
45-60	23.4		31.2		65.9		149.0		4351		128.3		57.4		36
30-45	26.2		27.6		36.1		64.5		129.7		318.2		91.4		30
15-30	32.6		35.4		50.3		85.1		126.1		168.7		138.2		30
0-15	50.3		49.6		69.5		102.1		128.3		114.8		88.6		30

(ψ, ϕ) elevation- resp. azimuth angle ($^\circ$)

$\Delta\phi$ azimuth increment ($^\circ$)

datapoints in $\text{W.m}^{-2}.\text{sr}^{-1}$

figure 5.6. Shortwave radiance distribution on a 'clear' day (light haze).

Figure 5.7 shows the corresponding calculated radiative temperatures (eq. 4.4).

The values given in figure 5.6 can be integrated over the hemisphere to give the irradiance at a horizontal plane and at the different orientated vertical surfaces.

A first approximation of the diffuse radiative components may be found by assuming that the irradiance at normal incidence S_n is found when the sun is within the field of view (this is only a crude assumption since an amount of diffuse radiation is produced in the direct surroundings of the sun). Integrating again, but now omitting direct solar

radiation leads to the diffuse components.

date			time (GMT)					spectral region				0° = north	
04-08-'81			11.00					0.3 ≤ μ ≤ 3 μm				90° = east	
φ	345	15	45	75	105	135	165	195	225	255	285	315	φ
ψ	15	45	75	105	135	165	195	225	255	285	315	345	$\Delta\varphi$
75-90	8200			8400			8200			8200			72
60-75	8400	8200	8000	8000	8000	8600	8400	8600	8600	8600	8600	45	
45-60	8400	8600	8600	7200	6000	8200	8000	7600	8000	8200	8200	36	
30-45	7400	8200	8000	7200	7800	5800	8800	7800	7200	7000	5400	7000	30
15-30	5800	6600	7000	7000	6800	6800	6800	7000	6200	5800	5600	5400	30
0-15	4000	4800	4900	4600	4800	5400	5600	4800	4400	4000	4000	4000	30

(ψ, φ) elevation- resp. azimuth angle (°)

$\Delta\varphi$ azimuth increment (°)

datapoints in K

figure 5.7. Radiative temperature distribution on a 'clear' day (light haze).

Using the solarimeter value as input parameter the different components may also be found using the equations given in section 3.1 (solar elevation- and azimuth angle are given in figure 5.3); table II shows the results.

There is a remarkable difference between the diffuse components found by measurement and calculation. The fact that the measured ones are considerably higher than the calculated ones may be caused by the hazy atmosphere (the synopsis of Volkel gives a horizontal visibility of 2800 m and 1/8 cloud coverage). A further suggestion in this direction is found from figure 5.7: the radiative temperatures are relatively low, again caused by low atmospheric transmissivity.

In the case of a clouded (or clear) sky, when no point source is present, the responsivity is approximated by a block-shape, using the half width (fig. 5.4); this results in an effective field of view of $15^\circ \times 15^\circ$. The consequence is that the irradiances have to be multiplied by a factor of 1.5.

date 4-8-'81		time (GMT) 11.00			spectral region $0.3 \leq \mu \leq 3 \mu\text{m}$		
description	'HDS'-value			using the equations given in section 3.1			
	direct	diffuse	total	direct	diffuse	total	
horizontal	502	273	775	565	170	735	
vertical, north	-	72	72	-	76	76	
east	122	126	247	120	109	229	
south	373	193	565	379	152	531	
west	-	113	113	-	84	84	

values are given in W.m^{-2}

global irradiance is 735 W.m^{-2} (fig. 5.1)

table II. Direct- and diffuse shortwave irradiance at surfaces of different orientations, during a 'clear' day.

Figure 5.8 and 5.9 show the radiance distribution and the corresponding radiative temperatures resp. at 09.00 GMT on 24 August 1981. (Since the raindetector broke down, the 'HDS' only could be used during clouded conditions in daytime).

date 24-08-'81		time (GMT) 09.00			spectral region $0.3 \leq \mu \leq 3 \mu\text{m}$			$0^\circ = \text{north}$ $90^\circ = \text{east}$							
ψ	ϕ	345	15	45	75	105	135	165	195	225	255	285	315	ϕ	
ψ	ϕ	15	45	75	105	135	165	195	225	255	285	315	345	$\Delta\phi$	
75-90		22.7		23.4		22.0		20.6		20.6				72	
60-75		34.8		39.0		41.1		41.1		42.5		39.0		38.3	34.8
45-60		41.1		50.3		67.3		75.1		60.9		54.6		48.2	42.5
30-45		41.8		50.3		58.1		61.7		73.0		60.2		46.1	51.7
15-30		44.6		48.9		51.7		48.2		58.9		44.6		40.4	43.9
0-15		38.3		37.6		40.4		40.4		46.1		38.3		36.1	34.0

(ψ, ϕ) elevation- resp. azimuth angle ($^\circ$)

$\Delta\phi$ azimuth increment ($^\circ$)

datapoints in $\text{W.m}^{-2}.\text{sr}^{-1}$

figure 5.8. Shortwave radiance distribution on an overcast day.

Weatherdata at this timepoint are: cloud coverage $7/8 - 8/8$ (cumulus and stratocumulus), horizontal visibility 20 km and air temperature 15.2 $^{\circ}\text{C}$.

date			time (GMT)				spectral region $0.3 \leq \mu \leq 3 \mu\text{m}$				0° = north 90° = east		
24-08-'81			09.00										
ψ	345	15	45	75	105	135	165	195	225	255	285	315	ψ
ψ	15	45	75	105	135	165	195	225	255	285	315	345	$\Delta\phi$
75-90	5400			5400			5400			5400			5200
60-75	5200		5400		5400		5400		5200		5400		5200
45-60	5200		5400		5200		5200		5200		5200		36
30-45	5000	5200	5000	5000	5200	5200	5000	5000	5200	5200	5000	5000	30
15-30	4800	4800	4800	4800	4800	4600	4800	4800	5000	5000	4800	4800	30
0-15	4000	4200	4200	4200	4200	4200	4000	4200	4000	4200	4000	4200	30

(ψ, ϕ) elevation- resp. azimuth angle ($^{\circ}$)

$\Delta\phi$ azimuth increment ($^{\circ}$)

datapoints in K

figure 5.9. Radiative temperature distribution on an overcast day.

Integrated results are shown in table III. The table shows that the irradiance at the vertical surfaces is about equal, implying that the cloudcover is rather homogeneous.

description		W.m^{-2}	date
horizontal		205 (*)	24-8-'81
vertical, north		78	time (GMT)
east		95	09.00
south		90	spectral region
west		77	$0.3 \leq \mu \leq 3 \mu\text{m}$

(*) solarimeter reading 216 (W.m^{-2})

table III. Direct- and diffuse shortwave irradiance at different orientated surfaces during an overcast day.

It is also seen that the east- and south surface receive a little more radiation and as can be seen from figure 5.8 the sun is not completely obscured (solar elevation and -azimuth are 38.4° resp. 126.7°) but the sun as such is not observable.

5.2.2 Longwave irradiance

Longwave irradiance in different wavelength intervals is measured parallel to the measurement of shortwave irradiance (section 4.2). The germanium filter used for broadband measurements, has the disadvantage that it cannot be used in daytime because it transmits radiation above $2.0\text{ }\mu\text{m}$ (about 5% of the solar-irradiance emitted in the wavelength region $0.3\text{-}3\text{ }\mu\text{m}$ falls within the spectral region $2\text{-}3\text{ }\mu\text{m}$). For a heavy overcast sky, like 24 August '81 the data are analyzed to see to what extend they might be useful. Figure 5.10 and 5.11 show the radiance distribution and the corresponding radiative temperatures at 09.00 GMT.

date 24-08-'81			time (GMT) 09.00						spectral region figure 4.9				0° = north 90° = east	
ψ	345	15	45	75	105	135	165	195	225	255	285	315	ψ	
ψ	15	45	75	105	135	165	195	225	255	285	315	345	$\Delta\phi$	
75-90	107.7			111.3			114.1			112.0			107.0	
60-75	100.6	107.7	109.8	111.3	114.1	114.1	109.8	109.1	102.8	45				
45-60	100.6	102.1	99.9	108.4	114.8	124.7	141.1	134.7	114.1	99.9	36			
30-45	94.3	103.5	113.4	119.1	131.1	118.4	102.1	107.0	107.7	101.3	89.3	97.1	30	
15-30	90.0	89.3	92.1	90.7	91.4	87.9	92.1	104.9	96.4	99.9	97.8	92.8	30	
0-15	86.5	87.2	88.6	87.9	94.3	86.5	85.0	84.3	82.9	82.2	84.3	87.9	30	

(ψ, ϕ) elevation- resp. azimuth angle ($^\circ$)

$\Delta\phi$ azimuth increment ($^\circ$)

datapoints in $\text{W} \cdot \text{m}^{-2} \cdot \text{sr}^{-1}$

figure 5.10. Longwave radiance distribution on an overcast day.

date 24-8-'81			time (GMT) 09.00				spectral region fig. 4.9				0° = north 90° = east		
φ	345	15	45	75	105	135	165	195	225	255	285	315	φ
ψ	15	45	75	105	135	165	195	225	255	285	315	345	Δφ
75-90	288		288		286		284		284		72		
60-75	280		284		286		288		286		286		45
45-60	280		288		302		304		296		290		280
30-45	276		282		288		292		300		292		276
15-30	274		278		280		276		282		274		272
0-15	270		270		270		276		270		268		268
							268	268	268		268		270
													30

(ψ, ϕ) elevation- resp. azimuth angle (°)

$\Delta\phi$ azimuth increment (°)

datapoints in K

Figure 5.11. Radiative temperature distribution on an overcast day.

From both figures it is seen that there is forward scattering in the neighbourhood of the sun (elevation- and azimuth angle 38.4° resp. 126.7°); the resulting values are somewhat too high due to the transparency of the germanium between 2 and 3 μm . Unfortunately this problem cannot be solved easily, because a filter blocking radiation below 3 μm and transmitting above 3 μm (up to 50 μm) by my knowledge does not exist; the best choice would be a filter made of indium arsenide as a base material, which transmits from 3.5 to about 10 μm , however the mean transmissivity is 0.5, so problems might arise with the signal to noise ratio if the radiation of a blue sky is measured.

Table IV shows the integrated results, also the integrated radiative 'sky' temperature θ_{as} is given.

date 24-8-'81	time (GMT) 09.00	spectral region fig. 4.9
description	$(\text{W} \cdot \text{m}^{-2})$	$\theta_{as} (\text{K})$
horizontal	333	277
vertical, north	148	269
east	162	275
south	157	273
west	148	269

table IV. Longwave irradiance at different orientated surfaces and the radiative 'sky'-temperature on an overcast day.

The longwave irradiance at a horizontal plane L (table IV) can be used to estimate the atmospheric emissivity $\bar{\epsilon}_a(c)$ or cloudbase temperature T_c ($\epsilon_c = 1$) from

$$L = \sigma \bar{\epsilon}_a(c) T_a^4 = \sigma \theta_c^4 \quad (\text{W} \cdot \text{m}^{-2})$$

where c cloud coverage ($^7/\text{s} - ^8/\text{s}$)

T_a ambient air temperature ($T_a = 288.2 \text{ K}$)

resulting in $\bar{\epsilon}_a(c) = 0.85$ or $\theta_c = 277 \text{ (K)}$.

These results are well in agreement with [1, 3].

At night we don't have to consider the problem concerning the germanium filter.

Figure 5.12 and 5.13 show the radiance distribution and the corresponding radiative temperatures on a clear night at 22.30 (GMT) on 7 July '81.

date 07-07-'81			time (GMT) 22.30						spectral region figure 4.9				0° = north 90° = east	
ψ	345	15	45	75	105	135	165	195	225	255	285	315	ψ	
ψ	15	45	75	105	135	165	195	225	255	285	315	345	$\Delta\phi$	
75-90	82.9			82.9			84.3			82.9			82.9	
60-75	85.0		84.3		85.0		85.0		84.3		85.0		85.0	45
45-60	88.6		87.2		87.9		88.6		87.2		87.9		87.2	36
30-45	93.5		92.8		93.5		92.1		92.8		92.8		93.5	30
15-30	103.5		103.5		103.5		103.5		102.8		102.0		102.8	30
0-15	121.9		121.9		121.9		123.3		121.2		120.5		121.2	30

(ψ, φ) elevation- resp. azimuth angle ($^\circ$)

$\Delta\varphi$ azimuth increment ($^\circ$)

datapoints in $\text{W.m}^{-2}.\text{sr}^{-1}$

figure 5.12. Longwave radiance distribution on a 'clear' night.

date 07-07-'81			time (GMT) 22.30						spectral region figure 4.9				0° = north 90° = east	
ψ	345	15	45	75	105	135	165	195	225	255	285	315	ψ	
ψ	15	45	75	105	135	165	195	225	255	285	315	345	$\Delta\phi$	
75-90	260			260			260			260			260	
60-75	262		262		262		262		262		262		262	45
45-60	264		264		264		264		264		264		264	36
30-45	268		268		268		268		268		268		268	30
15-30	274		274		274		274		274		274		274	30
0-15	286		286		286		286		286		286		286	30

(ψ, φ) elevation- resp. azimuth angle ($^\circ$)

$\Delta\varphi$ azimuth increment ($^\circ$)

datapoints in K

figure 5.13. Radiative temperature distribution on a 'clear' night.

Table V shows the integrated results. It is seen that the longwave 'sky'-irradiance at a vertical plane is independent of the azimuth angle and equals about half of the irradiance at a horizontal surface.

date	time (GMT)	spectral region fig. 4.9
7-7-'81	22.30	
description	(W.m ⁻²)	θ_{as} (K)
horizontal	305	271
vertical, north	165	275
east	164	275
south	165	275
west	166	275

table V. Longwave irradiance at different orientated surfaces on a 'clear' night.

The figures listed in table V can be compared with the results determined from the equations given in section 3.2 using the following meteorological data:

air temperature	287.7	(K)
relative humidity	0.98	
water vapor pressure	16.4	(mbar)

a. atmospheric emissivity $\bar{\epsilon}_a$ using mean values for α and β (eq. 3.5):

$$\bar{\epsilon}_a = 0.63 + 0.051 \sqrt{\epsilon} = 0.84$$

using the measured longwave irradiance at a horizontal plane L (table V) leads to:

$$\bar{\epsilon}_a = \frac{L}{\sigma T_a^4} = 0.79$$

This result is in good agreement with equation 3.5.

b. radiative 'sky'-temperature θ_{as} (eq. 3.6) using $\bar{\epsilon}_a = 0.84$

$$\theta_{as} = \left(\bar{\epsilon}_a\right)^{0.25} T_a = 275 \quad (\text{K})$$

This value is also in good agreement with the value found in table V.

c. Longwave irradiance at a horizontal plane L using $\bar{\epsilon}_a = 0.84$ is

$$L = \bar{\epsilon}_a \sigma T_a^4 = 326 \quad (\text{W.m}^{-2})$$

Compared to the measured value the error is about 7%.

Using some more clear night measurements showed a general agreement between measurements and calculations, using the Brunt type formula of equation 3.5. If it is assumed that the sky has a uniform temperature T_a equal to the ambient air temperature (measured at 1.5 m height), then the atmospheric emissivity ϵ_a as a function of elevation angle ψ is given by (eq. 3.3):

$$\epsilon_a(\psi) = a + b \sqrt{e} + c \ln[\sin \psi]$$

Atmospheric emissivity also can be determined from the long-wave sky radiance as a function of elevation angle $K_p(\psi)$:

$$\epsilon_a(\psi) = \frac{\pi K_p(\psi)}{\sigma T_a^4}$$

Figure 5.14 shows a comparison between these two methods, using the data at 22.30 GMT on 7 July 1981.

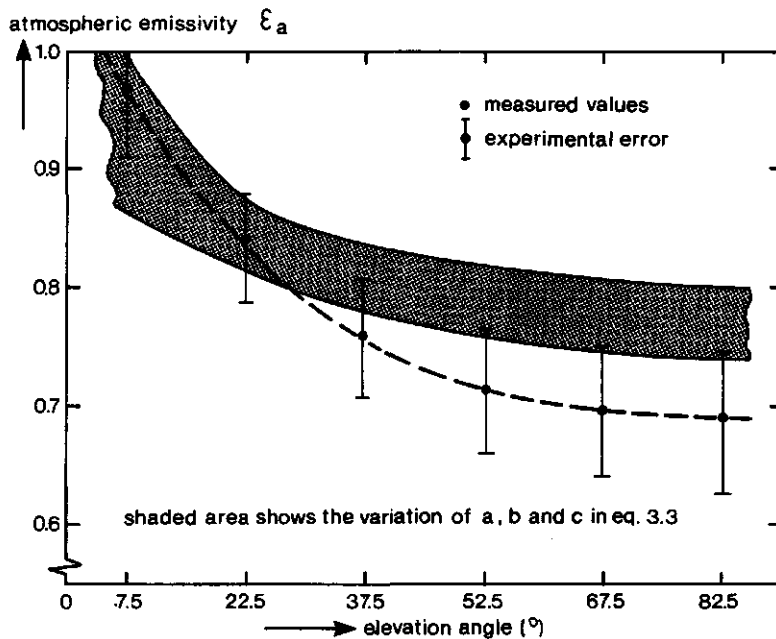


figure 5.14. Atmospheric emissivity as a function of elevation angle on a clear night.

Using an experimental error in $K_p(\psi)$ of 7% results in an error in the emissivity of

$$\frac{\Delta \epsilon_a(\psi)}{\epsilon_a(\psi)} = \frac{\Delta K_p(\psi)}{K_p(\psi)} = 7\%$$

or

$$\Delta \epsilon_a(\psi) = \pm 0.07 \epsilon_a(\psi)$$

Figure 5.14 also shows the variation of the coefficients a, b and c in eq. 3.3 using [3, 40]; the figure shows that the atmospheric emissivity in our case is lower at higher elevation angles. More measurements have to show whether this is systematic or not.

5.3 CONVECTIVE HEAT EXCHANGE

The convective heat exchange coefficient h is determined by

$$h = \frac{(Q_N - Q_6)}{(T_s - T_a)} = \frac{\Delta Q}{\Delta T} \quad (\text{W.m}^{-2}.\text{K}^{-1}) \quad (5.1)$$

wherein Q_N net irradiance at the surface (W.m^{-2})
 Q_6 heat flow through the surface (W.m^{-2})
 T_s surface temperature (K)
 T_a ambient air temperature measured
at 1.5 m height at about 20 m away
from the obstacle (K)

Equation 5.1 can be applied to different orientated surfaces for different atmospheric conditions.

The parameters in eq. 5.1 are available as measured quantities electronically averaged over a 10 minutes time interval. Q_N is measured for the entire surface while T_s and Q_6 are measured for each resolution element (fig. 4.2). Since these parameters have different time constants, one has to be careful using eq. 5.1 because strictly speaking it is only valid in the case of stationary heat exchange. Such conditions are met during a longer period of constant atmospheric conditions (i.e. constant wind velocity, solar-irradiance etc.). As an example of such a period the timeframe between 10.40 and 12.20 GMT on 6 August 1981 has been used to determine h . The mean windspeed \bar{v} in this period is $\bar{v} = 1.9 \pm 0.1 \text{ m.s}^{-1}$ and the mean wind direction is $\bar{\psi}_v = 45^\circ \pm 10^\circ$. Calculating h every 10 minutes shows that h is nearly constant, having a mean value \bar{h} over the whole period $\bar{h} = 25.6 \pm 1.5 \text{ W.m}^{-2}.\text{K}^{-1}$.

Since such periods are rather an exception than a rule another way of determining h has to be used: this is done by averaging the data over such a time period that the situation then found is approximately stationary. To determine

the averaging time, the time constants of the parameters in eq. 5.1 are determined. Figure 5.15 shows the time behaviour during a period where the sun is obscured by a cloud for only a short time while the windspeed and -direction are unchanged. As can be seen from this figure the surface temperature T_s has the largest time constant of about 20 minutes.

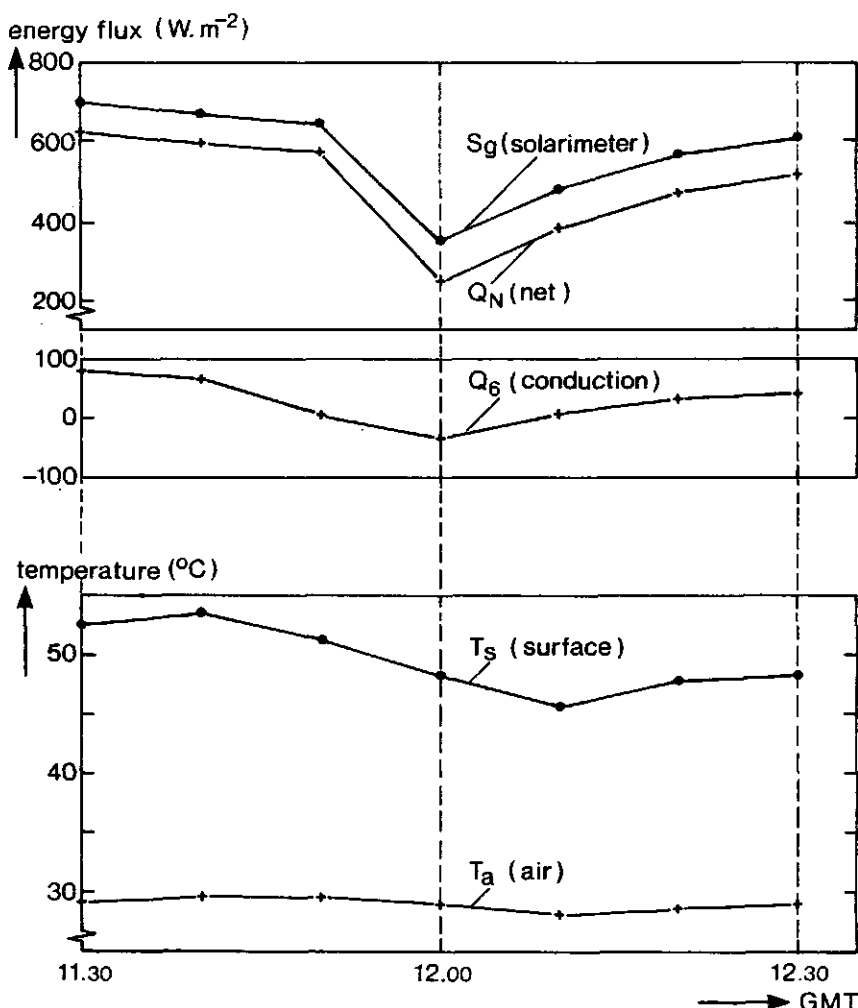


figure 5.15. Time behaviour of various parameters during a short period of obscuration of the sun by a cloud.

The averaging time has been set equal to the largest time constant i.e. 20 minutes. In practice this means that two values have to be averaged (data are available at 10 minutes interval); it is however not meaningful to average two successive datapoints if these figures differ to much in absolute value. For instance the average windspeed of 5 m.s^{-1} determined from two windspeeds of 9 and 1 m.s^{-1} only has little value.

As already explained in section 3.4 the heat exchange coefficient h will be related to the Reynolds number N_{Re} and to the wind direction ϕ_v . These parameters will determine the averaging process i.e. two successive windspeeds v_1 and v_2 are averaged if $(v_1 - v_2) \leq \pm 1 \text{ m.s}^{-1}$ and two successive wind directions $\phi_{v,1}$ and $\phi_{v,2}$ are averaged if $(\phi_{v,1} - \phi_{v,2}) \leq \pm 15^\circ$. The same kind of criteria could be formulated for all the parameters involved in the heat balance equation (eq. 1.3); this however is not done (except for the value of $\Delta T_m = T_s - T_a$) because one needs a very extensive data-base to have enough datapoints left for analyzing purposes.

The heat exchange coefficient h is determined by

$$h = a(N_{Re})^n f(\phi_v) \quad (\text{W.m}^{-2}.\text{K}^{-1}) \quad (5.2)$$

wherein a a constant $(\text{W.m}^{-2}.\text{K}^{-1})$

n a constant

ϕ_v wind direction measured at 1.5 m

height at about 20 m away from

the obstacle

$(^\circ)$

N_{Re} Reynolds number given by

$$N_{Re} = \frac{vL}{\nu}$$

wherein v windspeed measured at 1.5 m height

at about 20 m away from the obstacle (m.s^{-1})

L characteristic (scaling) length,

taken as half the perimeter of the

surface

(m)

I. The dependence of h on the Reynolds number N_{Re} for three different orientated surfaces

First equation 5.2 will be solved using a mean constant wind direction ϕ_v , in this case eq. 5.2 reduces to

$$h = b(N_{Re})^n \quad (W \cdot m^{-2} \cdot K^{-1}) \quad (5.3)$$

Knowing ϕ_v a search can be made through the data to look for timepoints where ϕ_v equals the actual one, then h and N_{Re} are determined. During this search some criteria have to be met before a datapoint is accepted:

1. no precipitation allowed one full hour preceding the datapoint found.
2. the difference between air- and surface temperature has to be larger than a given minimum ΔT_m . This is done to prevent that the nominator in eq. 5.1 gets too small and also to be sure that the convective term itself is not too small.

This procedure is applied to the different obstacle walls, using several wind directions ϕ_v :

A. Top surface

Since the data-base is not very extensive, not many datapoints are accepted if the criteria get to powerful. As an example figure 5.16 shows a graphical representation of eq. 5.3 for different wind directions. The figure also shows the constants b and n (eq. 5.3) and the root mean square value (rms) using a least square approximation. The minimum temperature difference ΔT_m can be varied to find an optimum curve fit; this is the case when the root mean square error is the smallest and the number of datapoints is still large enough to do the curve fitting. Doing so, a value of $\Delta T_m = 8$ K was found.

Figure 5.17 shows the results, showing that the rms-values have come down.

symbol	ϕ_v (°)	$b \times 10^2$ (W.m ⁻² .K ⁻¹)	n	rms (W.m ⁻² .K ⁻¹)
—○—	240	0.23	0.69	2.9
—●—	250	4.19	0.48	4.0
—+—	260	4.02	0.48	3.5
—■—	270	0.93	0.59	4.9

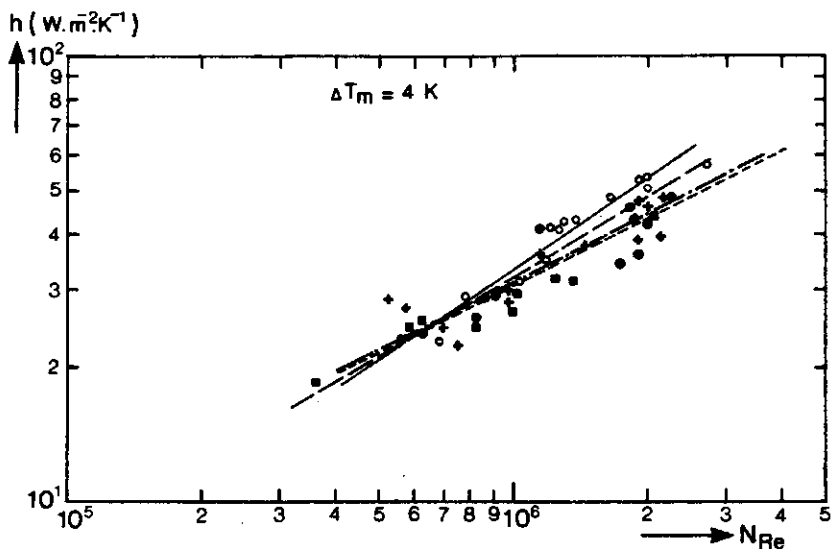


figure 5.16. Relation between the heat exchange coefficient h and the Reynolds number N_{Re} for the topsurface for different wind directions ϕ_v .

The exponent n ranges between 0.5 and 0.7. This result is in agreement with those reported in [32], using spheres placed in an outdoor environment. The same source learns that there is a considerable variation in the data, probably due to the stochastic behaviour of the wind over different test periods. The relative spread in the data over the different wind directions may also be generated by a variation of turbulence intensity as a function of wind direction; in [32] and [36] an enhancement in heat transfer was found

to be caused by an increase of turbulence intensity.

symbol	ϕ_v (°)	$b \times 10^2$ ($\text{W} \cdot \text{m}^{-2} \cdot \text{K}^{-1}$)	n	rms ($\text{W} \cdot \text{m}^{-2} \cdot \text{K}^{-1}$)
—○—	240	0.13	0.73	2.6
—●—	250	1.03	0.58	1.1
—+—	260	9.43	0.41	2.3
—■—	270	3.65	0.49	1.0
mean values		1.5	0.55	1.6

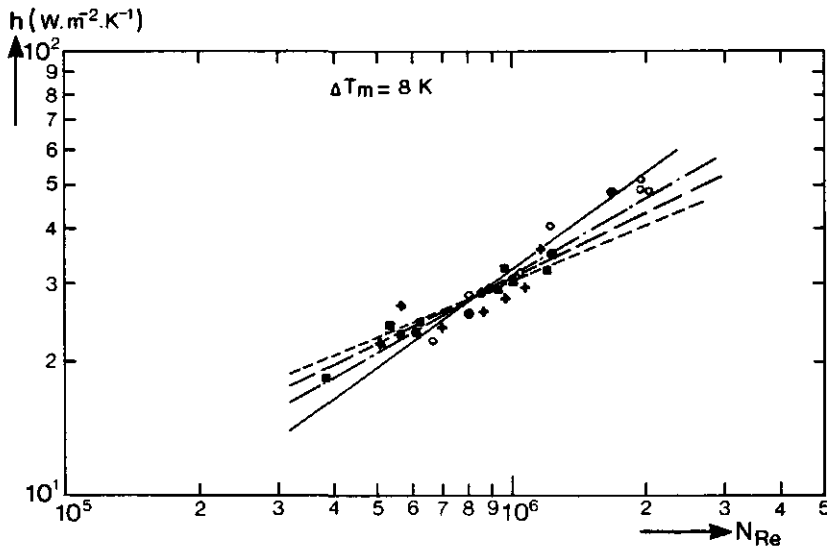


figure 5.17. Relation between the heat exchange coefficient h and the Reynolds number N_{Re} for the topsurface for different wind directions ϕ_v .

B. West surface

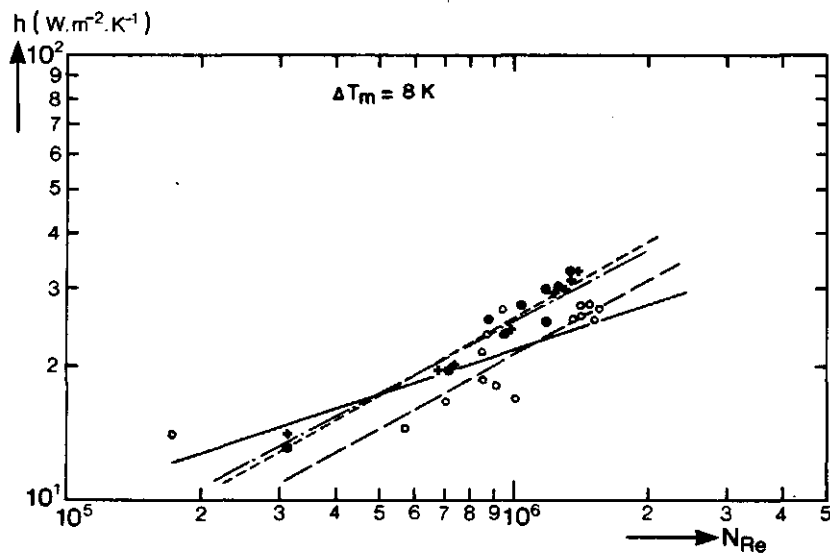
During westerly winds, in general the weather was not so nice, leaving not many datapoints to be accepted.

Figure 5.18 shows the relation between h and N_{Re} using

$$\Delta T_m = 8 \text{ K.}$$

The number of datapoints is quite small and the influence of an individual datapoint can be large. For instance this is the case for $\phi_v = 40^\circ$, where there is a datapoint ($h, N_{Re} = 14, 1.7 \cdot 10^5$) which falls clearly outside the range formed by the remaining datapoints.

symbol	ϕ_v ($^\circ$)	$b \times 10^2$ ($\text{W.m}^{-2} \cdot \text{K}^{-1}$)	n	rms ($\text{W.m}^{-2} \cdot \text{K}^{-1}$)
—●—	220	1.2	0.55	1.8
—+—	230	0.72	0.59	1.2
—○—	40	17.7	0.35	3.0
— — —	40*	0.78	0.58	2.6
mean values 1)		0.87	0.57	1.9



1) excluding $\phi_v = 40^\circ$

figure 5.18. Relation between the heat exchange coefficient h and the Reynolds number N_{Re} for the west surface for different wind directions ϕ_v .

Tracing back the date and time of this datapoint, revealed that it was taken in the late evening after a warm sunny day. At that time windspeed was 0.4 m.s^{-1} , surface temperature 45°C and the air temperature 22°C . These values indicate that free convective heat transfer is the main heat exchange mechanism.

Omitting this point in the analysis, gives a result comparable to the value of n found in other situations (fig. 5.18, $\psi_v = 40^*$).

This again shows that the datapoints have to be chosen very carefully.

C. North surface

Since the temperature difference ΔT_m in this case nearly always is very small (only little solar irradiance) not many datapoints are being left for evaluation. Using anyway the best circumstances, data are still quite scattered. Figure 5.9 shows the relation between h and N_{Re} using $\Delta T_m = 3 \text{ K}$. Again there is an indication that the exponent n is within the same range as before i.e. $0.5 < n < 0.7$.

Because the influence of only one datapoint can be large and also because of the natural spread in the wind direction of $\pm 15^\circ$, it is unlikely that the differences found between the regression curves is significant. Therefore mean values have been determined from the values given for each surface. Looking to these figures reveal that there is hardly any difference between the *mean* rms-value and the rms-values for the *individual* regression curves (mean rms-values even are somewhat smaller).

A mean value for $\bar{n} = 0.55$ seems to be appropriate in the situations investigated.

symbol	ϕ_v (°)	$b \times 10^2$ (W.m ⁻² .K ⁻¹)	n	rms (W.m ⁻² .K ⁻¹)
-----●-----	230	3.3	0.47	3.0
-----+-----	270	1.6	0.53	3.0
mean values		2.2	0.50	1.6

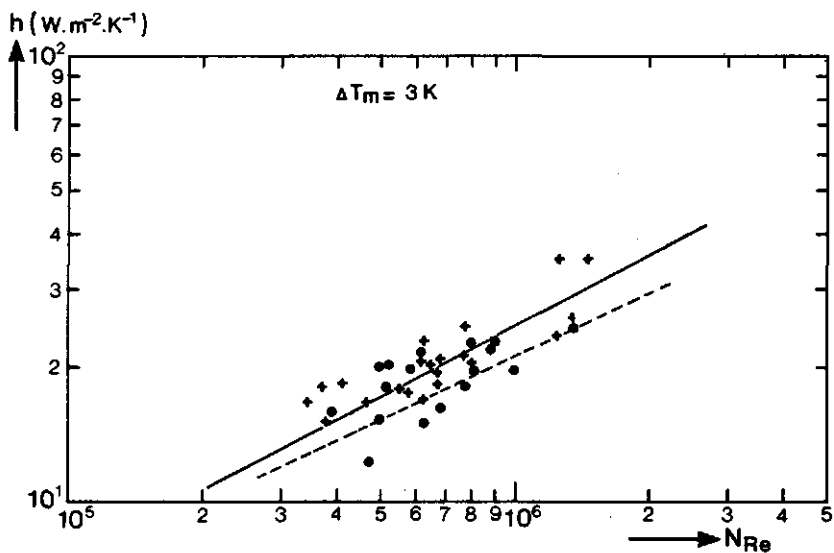


figure 5.19. Relation between the heat exchange coefficient h and the Reynolds number N_{Re} for the north surface for different wind directions ϕ_v .

II. The dependence of h on the wind direction ϕ_v for three different orientated surfaces

Next the relation between h and wind direction ϕ_v will be discussed:

$$h = c f(\phi_v) \quad (\text{W.m}^{-2} \cdot \text{K}^{-1}) \quad (5.4)$$

Eq. 5.4 can be solved using different windspeeds; results are given for $0^\circ < \phi_v \leq 360^\circ$. In fact only wind directions of $270^\circ \pm 90^\circ$ should be used since terrain roughness in that sector is more or less constant, however covering the entire range gives a better overview and makes the behaviour within the sector more understandable.

In this case it is not possible to calculate something as a root mean square error since the relation $h(\phi_v)$ is not known. The previous analysis showed however that increasing ΔT_m in general decreases the rms-value, so in this case the same value for ΔT_m can be adopted.

A. Top surface

Figure 5.20 shows the measurements for a mean windspeed $v = 2 \text{ m.s}^{-1}$ and $v = 4 \text{ m.s}^{-1}$ using $\Delta T_m = 8 \text{ K}$. It was expected that there would be some symmetry in the figure, since the top surface is a rectangle with dimensions which differ by a factor of 2.

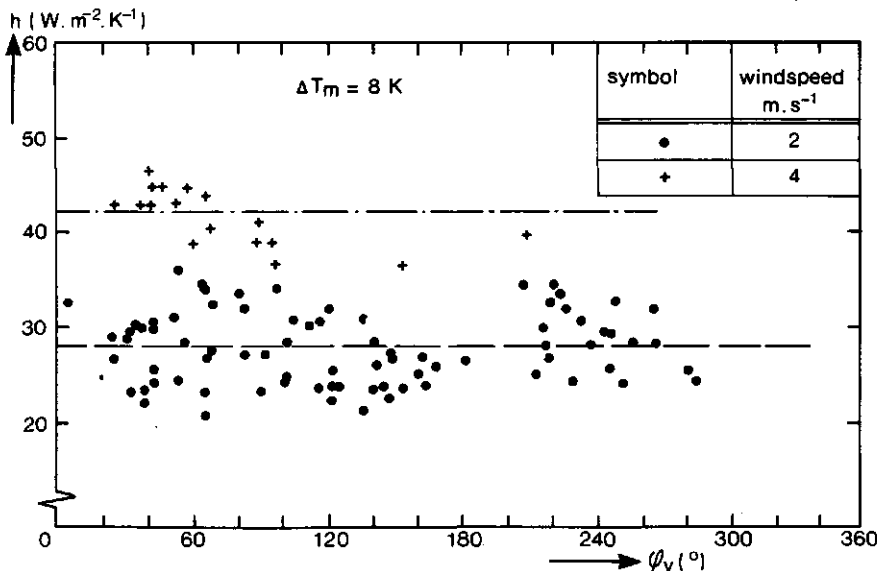


figure 5.20. Relation between the heat exchange coefficient h and the wind direction ϕ_v for the topsurface for two different windspeeds.

Due to the spread in the datapoints this is not noticeable; changing the windspeed to $v = 2 \pm 0.5 \text{ m.s}^{-1}$ did not change the figure very much (only more datapoints). This means that the spread due to 'other' influences is larger than due to the change in windspeed. Since all angle dependence is washed out by this spread, a linear relationship is assumed; the resulting mean heat exchange coefficient \bar{h} is shown in table VI.

v (m.s^{-1})	\bar{h} ($\text{W.m}^{-2}.\text{K}^{-1}$)	rms ($\text{W.m}^{-2}.\text{K}^{-1}$)	$\Delta v = \pm 0.5 \text{ (m.s}^{-1}\text{)}$
2.0	28.1	3.5	
3.0	34.5	4.7	
4.0	41.0	2.9	
5.0	44.3	2.5	

table VI. Relation between the windspeed v and the mean heat exchange coefficient \bar{h} for the topsurface.

The order of magnitude of the rms-value is about the same as in the relation between h and N_{Re} . This value is reduced if only the data within $\phi_v = 270^\circ \pm 90^\circ$ are considered in the analysis.

Using a mean exponent $\bar{n} = 0.55$ together with the values listed in table VI (thus assuming $f(\phi_v) = \text{constant}$), the coefficient b in eq. 5.3 can be determined; table VII shows the results.

v (m.s^{-1})	\bar{h} ($\text{W.m}^{-2}.\text{K}^{-1}$)	$b \times 10^2$ ($\text{W.m}^{-2}.\text{K}^{-1}$)	$\Delta v = \pm 0.5 \text{ (m.s}^{-1}\text{)}$ mean value for b :
2.0	28.1	1.59	
3.0	34.5	1.57	
4.0	41.5	1.59	$\bar{b} = 1.56 \times 10^{-2} \text{ (W.m}^{-2}.\text{K}^{-1}\text{)}$
5.0	44.3	1.52	$\text{rms} = 0.03 \times 10^{-2} \text{ (W.m}^{-2}.\text{K}^{-1}\text{)}$

table VII. The variation of the coefficient b in eq. 5.3 as a function of windspeed v .

Best fit using the mean coefficients is

$$h = 0.0156 N_{Re}^{0.55} \quad (W.m^{-2}.K^{-1})$$
$$rms = 2.9 \quad (W.m^{-2}.K^{-1})$$

B. West surface

The heat exchange coefficient shows a maximum for $\phi_v = 180^\circ$ and a minimum for $\phi_v = 270^\circ$. Figure 5.21 shows this behaviour for $v = 2 \text{ m.s}^{-1}$ and $\Delta T_m = 6 \text{ K}$.

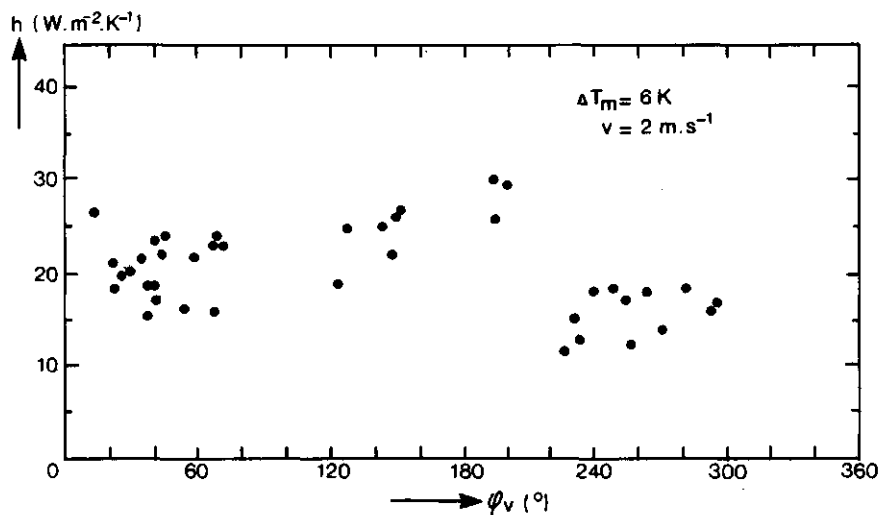


figure 5.21. Relation between the heat exchange coefficient h and the wind direction ϕ_v for the west surface.

It is seen that when approaching the surface from the leeward side on to the windward side, the convective heat exchange is increasing, having a maximum at about $\phi_v = 180^\circ$. This behaviour is also found in literature [10]. A reason could be the production of turbulent vortices at the leeward side.

C. North surface

Again one has to be careful with the data; but there is an indication that two maxima exist; these occur when the wind is parallel to the surface i.e. $\phi_v = 270^\circ$ and $\phi_v = 90^\circ$. Figure 5.22 shows the relation between h and ϕ_v where $v = 2 \text{ m.s}^{-1}$ and $\Delta T_m = 3 \text{ K}$.

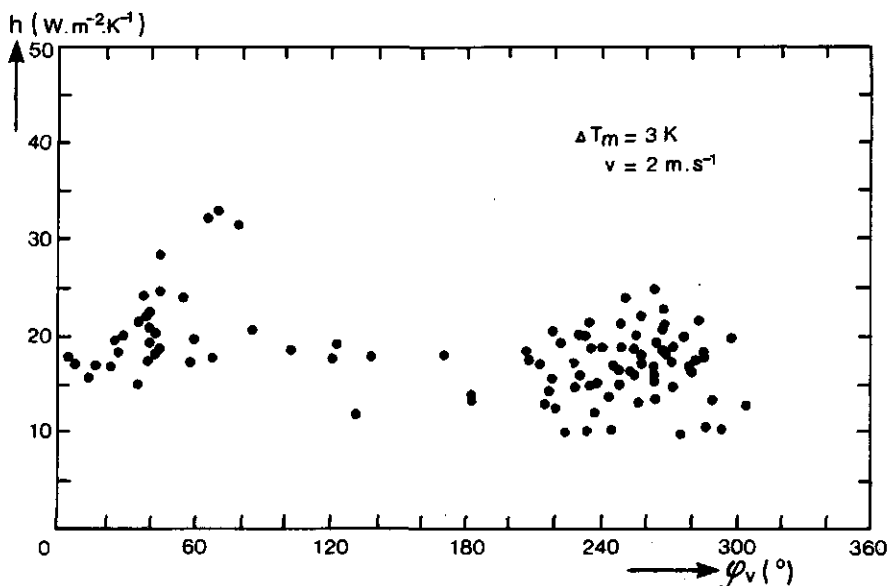


figure 5.22. Relation between the heat exchange coefficient h and the wind direction ϕ_v for the north surface.

The location of these maxima however is so uncertain that no conclusions can be drawn.

5.4 RADIATIVE CHARACTERISTICS

IR-detectability depends on the prevailing contrasts and the system performance (temperature- and geometrical resolution). This contrast can be expressed in terms of a difference in radiative temperature $\Delta\theta_s$ or in terms of a difference in apparent emittance ΔG_s .

The contrast can be found by solving the radiation balance of a surface or it can be measured directly using a radiometer, in this case the 'ELSCA'.

For evaluation purposes the same days are used as have been used in the previous section. The amount of IRLS*) overflights was very limited. The International Training Centre (ITC) only was able to perform two missions, one on 22 June and the other on 18 August. When the last overflight was performed luck left us because several systems broke down due to power failure on the airbase; therefore no quantitative analysis of the IR-imagery is possible.

The irradiance at the entrance pupil L_p of the scanner is given by (eq. 3.10 and fig. 3.9):

$$L_p = \frac{1}{\pi} \int_{A_1} \int_{A_2} \frac{\cos \nu_d}{R^2} dA_1 dA_2 \int_{\mu_0} G_s(\mu, T_s) \tau_a(\mu) d\mu \quad (W \cdot m^{-2})$$

For a scanner looking straight down ($\nu_d = 0^\circ$), L_p can be written as

$$L_p \sim \int_{\mu_0} G_s(\mu, T_s) \tau_a(\mu) d\mu \quad (W \cdot m^{-2}) \quad (5.5)$$

*) Infrared line scanner

The spectral atmospheric transmissivity τ_a shows two regions where the atmosphere is transparent i.e. 3-5 and 8-14 μm (fig. 1.3).

This implies that for IR-observations, the radiative properties within these area's are of main interest. Since for bodies at ambient temperatures peak emittance is at 10 μm , most systems use the 8-14 μm window.

If it is assumed that the atmospheric transmissivity τ_a is constant within this window, then eq. 5.5 reduces to

$$L_p \sim \int_8^{14} G_s(\mu) d\mu \quad (\text{W.m}^{-2})$$

The spectral apparent emittance G_s of a horizontal surface is

$$G_s(\mu) = \epsilon_s(\mu) W(\mu, T_s) + \rho_\ell(\mu) L(\mu) \quad (\text{W.m}^{-2}) \quad (5.6)$$

For a vertical surface, terrain influence has to be incorporated.

For many materials the spectral reflectivity varies as for the green paint used on the obstacle (fig. 5.23).

The IR-reflectometer has not been used in the field yet.

It was however used in the laboratory on different materials and paints [38]. Aluminium foil was used as a 100% reflectivity standard.

These measurements showed a good agreement with literature [23] and also with other measurement techniques, whereby the specimen was heated and the reflectivity was found from the real- and radiative temperature.

Measurements showed that the sample surface is irradiated diffusely by the black bodies and that in turn the detector is also irradiated diffusely (if the sample surface is a diffuse reflector).

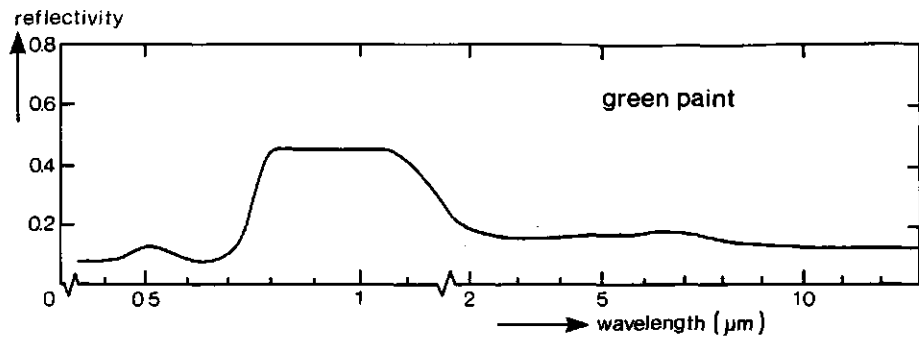


figure 5.23. Spectral reflectivity of the green paint used on the obstacle.

The apparent emittance G_s is measured directly in different wavelength intervals (p. 61), using the scanning radiometer 'ELSCA'. The quantity measured with the 'ELSCA', Q_{el} is found from:

$$Q_{el} = \underbrace{\int_{\mu_0}^{\infty} \epsilon_s W(\mu, T_s) d\mu}_{\substack{\text{I: surface} \\ \text{emittance}}} + \underbrace{\int_{\mu_0}^{\infty} \rho_\ell L(\mu) d\mu}_{\substack{\text{III: reflected} \\ \text{sky-irradiance}}} \quad (\text{W.m}^{-2}) \quad (5.7)$$

wherein μ_0 spectral interval given by fig. 4.9.

Table VIII shows the terms in eq. 5.7 applied to the top-surface at different days. Mean longwave reflectivity $\rho_\ell = 0.10$ has been used.

The table shows that Q_{el} and $(I + III)$ are well in agreement; Q_{el} is slightly lower (3-6%).

At nighttime longwave downward irradiance at a horizontal surface may also be found from

$$L = Q_N + Q_{el} \quad (\text{W.m}^{-2})$$

wherein Q_N net-irradiance at the surface $(W.m^{-2})$

date	time (GMT)	T_a (K)	T_s (K)	Q_{el} ($W.m^{-2}$)	I ($W.m^{-2}$)	III ($W.m^{-2}$)
4-8-'81	11.00	299.2	321.2	543	542	37 ¹⁾
24-8-'81	09.00	288.2	296.3	407	393	33 ²⁾
7-7-'81	22.30	287.7	288.1	367	351	30 ³⁾

$$1) \quad III = \rho_\ell (\bar{\epsilon}_a \sigma T_a^4) = \rho_\ell 370 = 37 \text{ } W.m^{-2}$$

$$2) \quad \text{table IV: } \rho_\ell L = \rho_\ell 333 = 33 \text{ } W.m^{-2}$$

$$3) \quad \text{table V: } \rho_\ell L = \rho_\ell 305 = 30 \text{ } W.m^{-2}$$

table VIII. Radiative quantities, measured at three different days.

At 22.30 GMT on 7 July 1981 using $Q_N = -42 \text{ } W.m^{-2}$ this leads to

$$L = -42 + 367 = 325 \text{ } (W.m^{-2})$$

compared to $L = 305 \text{ } W.m^{-2}$ found with the 'HDS'.

From these figures it is concluded that the 'ELSCA'-measurements are a good measure of the apparent emittance of a surface. From these measurements the radiative temperature or a difference in radiative temperature can be determined for different background elements. Table IX shows the radiative temperatures θ_s for different surfaces (the feature numbers correspond with those given in figure 4.23) on 4 August at 11.00 GMT. The radiative temperature is determined from the irradiance Q_{el} measured by the 'ELSCA' (using the germanium filter):

$$\theta_s = \left(\frac{\theta_{el}}{\sigma} \right)^{0.25} \quad (K)$$

The table also shows the radiative temperature contrast $\Delta\theta$ between the top surface θ_s and the other features θ_f i.e. $\Delta\theta = \theta_s - \theta_f$.

feature	θ_s (K)	$\Delta\theta$ (K)
1	307	+5
2	308	+4
3	299	+13
4	298	+14
5	308	+4
6	317	-5
7	311	+1
8	312	0
9	311	+1
10	311	+1

table IX. Radiative temperature θ_s and radiative temperature difference $\Delta\theta$ between the topsurface and some features (fig. 4.23), measured with the 'ELSCA' on a 'clear' day.

Table X shows the same parameters in case of an overcast sky on 24 August at 09.00 GMT. In this case the contrasts are much more moderate than on 4 August, but are still positive. Table XI shows the situation at nighttime on 7 July at 22.30 GMT, air temperature $T_a = 287.7$ (K). In this case negative- and positive contrasts occur.

feature	θ_s (K)	$\Delta\theta$ (K)
1	289	+2
2	290	+1
3	288	+3
4	286	+5
5	290	+1
6	291	0
7	291	0
8	291	0
9	289	+1
10	289	+1

table X. Radiative temperature θ_s and radiative temperature difference $\Delta\theta$ between the topsurface and some features (fig. 4.23), measured with the 'ELSCA' on an overcast day.

feature	θ_s (K)	$\Delta\theta$ (K)
1	282	+2
2	283	+1
3	281	+3
4	283	+1
5	283	+1
6	285	-1
7	287	-3
8	284	0
9	285	-1
10	285	-1

table XI. Radiative temperature θ_s and radiative temperature difference $\Delta\theta$ between the topsurface and some features (fig. 4.23), measured with the 'ELSCA' on a 'clear' night.

6.0 CONCLUSIONS AND RECOMMENDATIONS

The terms in the heat balance equation of a surface will be discussed separately. System performance and the first results obtained from a test-period will be summarized briefly.

A. Shortwave radiation

Shortwave radiance distribution of the sky had to be measured. For this purpose an instrument, called 'HDS' with a geometrical resolution of $15^\circ \times 15^\circ$ was developed. A complete scan of the hemisphere is performed in 3 minutes. Calibration of this instrument was done with a tungsten filament source, centered in the field of view.

Out in the field the 'HDS' was placed on a platform (7 m height); repetition time was 10 minutes with a maximum storage capacity of 25 hours. In the test period mainly data of 'clear' sky and overcast sky were collected:

1. 'Clear' sky

Since it was not possible to compare the measured sky-radiance distribution with other measurements, the irradiance at a horizontal plane was calculated using the measured sky-radiance distribution and compared with the global irradiance. The calculated values showed a periodical time behaviour; this is explained by the fact that the responsivity of the detector is not constant within the field of view. A maximum signal is detected when the sun is centered in the field of view, a minimum value occurs at the boundaries. The calculated irradiance at a horizontal plane using the situations where the sun was located in the centre of the field of view was in good agreement with the measured global irradiance. If the solar elevation angle is known the direct- and diffuse irradiance at a horizontal surface can be calculated from the global irradiance using [18]. Comparison with the measurements showed that the calculated direct irradiance at a horizontal plane was much smaller and that the calculated diffuse irradiance at a horizontal plane was much larger than the measured values. A possible reason for this is the

presence of a light haze during the measurements (visibility 2800 m).

2. Overcast sky

During overcast conditions measured global irradiance was in good agreement with the global irradiance determined from the sky-radiance distribution. It also appeared that the sky-irradiance at a vertical surface is roughly half of the global irradiance, independent of the surface azimuth angle.

A basic problem using the 'HDS' is that no direct comparison can be made with other measurements. The main measurement campaign will include a pyrheliometer to compare directly the radiance measured with both instruments.

To check for the irradiance at a vertical plane it may be worthwhile to include a solarimeter used in a vertical position; in this case reflected radiation by the terrain has to be measured (or to be estimated).

To increase system performance some characteristics have to be changed, but considering the effort it would be better to built a complete new system; a main task then is to make an instrument independent of the sun's position within the field of view.

B. Longwave radiation

Longwave sky-radiance distribution and shortwave sky-radiance distribution were measured simultaneously combined in one instrument. Geometrical resolution of the IR-detector also equals $15^\circ \times 15^\circ$, build parallel to the shortwave 'channel'.

No measurements were available to which 'HDS'-data directly could be compared to. To be able to compare the measurements with empirical relations given in literature, the longwave irradiance at different orientated surfaces is calculated using the measured radiance distribution.

1. Clear sky

The radiance distribution K_p is found to be independent on azimuth angle. Longwave sky-irradiance at a vertical surface L_v of arbitrary orientation is related to the irradiance at a horizontal surface L_h by

$$L_v = b L_h \quad (W \cdot m^{-2}) \quad (6.1)$$

wherein $b \approx 0.5$

At nighttime the longwave irradiance at a horizontal surface can be calculated from the net-irradiance at the surface and the apparent emittance (i.e. the sum of emitted and reflected radiation). There is a good agreement between this 'indirect' method and the 'direct' method using the 'HDS'-values. If it is assumed that the sky has a uniform temperature equal to the ambient air temperature T_a (measured at 1.5 m height) the atmospheric emissivity ϵ_a as a function of elevation angle ψ is

$$\epsilon_a(\psi) = \frac{\pi K_p(\psi)}{\sigma T_a^4}$$

Results indicate a lower value for ϵ_a at higher elevations than those reported in literature [3, 40]. More measurements have to show whether this is systematic or not.

2. Overcast sky

Longwave sky irradiance at a horizontal surface, determined from the radiance distribution is well in agreement with [1, 3] the value of b in eq. 6.1 does not significantly differ from 0.5. The actual value of 0.55 may be slightly too high because the sun was not completely obscured by the clouds resulting in a small contribution due to the

transparency of the germanium filter in 2-3 μm .

Again the problem arises that no direct comparison between the sky-radiance distribution and other measurements can be made. During the measurement campaign a pyrgeometer, measuring the longwave irradiance at a horizontal plane will be used to compare to the value found from the sky-radiance distribution.

C. Convective heat exchange

The convective heat exchange coefficient h for three surfaces of different orientation was calculated from

$$h = \frac{\Delta Q}{\Delta T} \quad (\text{W.m}^{-2}.\text{K}^{-1}) \quad (6.2)$$

wherein ΔQ the difference between the net-irradiance at the surface and the heatflow through the surface

ΔT the difference between the surface temperature and ambient air temperature measured at 1.5 m height at 20 m away from the obstacle.

Equation 6.2 has been related to the wind direction ψ_v and to the Reynolds number N_{Re} determined at 1.5 m height at 20 m away from the obstacle; half the perimeter of a surface was adopted as a scaling length.

1. The relation with the Reynolds number N_{Re}

Data were fitted to the equation

$$h = a N_{\text{Re}}^n \quad (\text{W.m}^{-2}.\text{K}^{-1})$$

For the horizontal surface as well as for the vertical surfaces

the exponent n ranges from 0.5-0.7, with a mean value of $\bar{n} = 0.55$. The value of n depends on the wind direction.

2. The relation with the wind direction ϕ_v

It was anticipated that the convective heat exchange coefficient for the topsurface would depend on the wind direction, however this was not found. An explanation for this, could be spread of the measurements due to the stochastic behaviour of the wind. Best fit for the topsurface gives a mean value for \bar{h} as

$$\bar{h} = 0.016 N_{Re}^{0.55} \pm 2.9 \quad (\text{W.m}^{-2}.\text{K}^{-1})$$

For the vertical surfaces there seems to be a dependence on the wind direction, the significance of this behaviour can only be determined if more data are available.

During the main measurement program it is necessary to change the polythene spheres of the net-radiometers much more frequently, to minimize transmission losses due to atmospheric influences.

It also will be possible then to study the influence of atmospheric turbulence intensity on the heat exchange coefficient.

To make it possible to measure the convective heat exchange at a windward- and leeward surface *at the same time*, the east surface will be included as measuring surface.

D. Radiative properties

In order to measure the apparent emittance (i.e. the sum of the emittance of - and reflected radiation at a surface) of different obstacle walls and of different terrain features a scanning radiometer, called 'ELSCA' was developed. This instrument, having a field of view of $2^\circ \times 2^\circ$ was placed on a platform 7 m above ground level. The results were well in agreement with the measurements of the individual

components forming the apparent emittance. This parameter is a measure of the angular irradiance at the aperture of an airborne scanner.

Apart from the surface temperature, the surface emittance is determined by the surface emissivity. A reflectometer [38] used to measure spectral longwave reflectivity of surfaces broke down during the test period. After finishing the repair work, it was used in the laboratory on different man-made materials. The reflectivity also was determined from radiometric measurements; results from both measurements were in good agreement.

Infrared aerial imagery was taken during a number of test flights using two scanners one with a high geometrical resolution ($1 \times 1 \text{ m}^2$ on the ground) and one with a high temperature resolution (0.01 K); image quality was good. During the measurement campaign ground based data will be used to get a better understanding of what is seen on the imagery.

REFERENCES

- [1] Monteith, J.L.
Principles of environmental physics
Edward Arnold limited, London (1973).
- [2] Jakob, M.
Heat transfer, Volume I and II
John Wiley & Sons, Inc., New York (1965).
- [3] Unsworth, M.H. and J.L. Monteith
Long wave radiation at the ground
I. Angular distribution of incoming radiation
II. Geometry of interception by slopes, solids and
obstructed planes
Q.J.R. met. Soc., 101, 13 (1975).
- [4] Gray, W.A. and R. Müller
Engineering calculations in radiative heat transfer
Pergamon Press Ltd., Oxford (1974).
- [5] Bell, E.E.
J. Opt. Soc. Am., 50, 1313 (1960).
- [6] Basset, C.R. and M.D.W. Pritchard
Environmental physics; heating
J.W. Arrowsmith Ltd., Bristol (1969).
- [7] S.T. Henderson
Daylight & its spectrum
Adam Hilger Ltd., Bristol (1977).
- [8] Jacobs, P.A.M.
Simulation model to calculate the surface temperature
of an asphalt layer
PHL 1976-32, TNO, The Hague, Netherlands (1978).

[9] Jacobs, P.A.M.
Simulation of the thermal behaviour of an object and its nearby surroundings
PHL 1980-08, TNO, The Hague, Netherlands (1980).

[10] Deventer, H.C. van
Hoekafhankelijkheid van konvektief warmtetransport
PHL 1978-12, TNO, The Hague, Netherlands (1978).

[11] Fuji, T. and H. Imura
Natural convection heat transfer from a plate with arbitrary inclination
Int. J. Heat Mass. Transfer, 15, 755 (1972).

[12] Howell, J.
Monte Carlo applications in heat transfer
Advances in heat transfer, 5, 1 academic press, New York (1968).

[13] Love, T.J.
Radiative heat transfer
Merril, Columbus (1968).

[14] Quick, F.
Thermal IR in geology
Photogrammetric engineering & remote sensing, 341 (1975).

[15] Robinson, N.
Solar radiation
Elsevier, Amsterdam (1966).

[16] Schmidt, E. und W. Beckmann
Das Temperatur- und Geschwindigkeitsfeld van einer Wärme abgebenden senkrechte Platte bei natürlicher Konvektion Teil I und II
Tech. Mech. u. Ther., 10, (1930).

[17] Selby, J.E.A. and R.M. Mc Clatchey
Atmospheric transmittance from 0.15-28.5 μm
Computercode LOWTRAN 2, AFCRL-TR-75-0255, 7 May 1975
Environmental research papers, no. 513.

[18] Bruggen, R.J.A. van der
Energy consumption for heating and cooling in relation
to building design
Ph.D. Thesis, Eindhoven University of Technology (1978).

[19] M.J.J. Roos
Beschrijving van Elsca, een elevatie-scannende radio-
meter
IR 1975-21, TNO, The Hague, Netherlands (1975).

[20] Lewis, R.W. and Morgan, K.
Numerical methods in thermal problems
Pineridge Press, Swansea UK (1979).

[21] Carslaw, H.S. and Jaeger, J.C.
Conduction of heat in solids
Oxford at the Clarendon Press (1959).

[22] Becherer, R.J.
Optical radiation measurements
Academic Press, New York, Volume 1 (1979).

[23] Weast, R.C.
Handbook of chemistry and physics
CEC Press (1975).

[24] Threlkeld, J.L.
Thermal environmental engineering
Prentice Hall, Inc. (1977).

[25] Bennet, H.E. et. al.
Distribution of Infrared Radiance over a clear sky
J. Opt. Soc. Am., 50, 100 (1960).

[26] Binnekamp, D. en Jong, A.N. de
Meting van de transmissie van de atmosfeer op lage
hoogten boven zee
IR 1976-26, TNO, The Hague, Netherlands (1976).

[27] Jong, A.N. de
Long-range transmission over sea water
PHL 1978-08, TNO, The Hague, Netherlands (1978).

[28] Hackforth, H.L.
Infrared radiation
Mc. Graw-Hill Book Company, Inc. (1960), p. 47.

[29] Jong, A.N. de
Een twee-kleuren vliegtuigscanner (project Floris)
PHL 1966-21, TNO, The Hague, Netherlands (1966).

[30] Jong, A.N. de
Description of an infrared scanner with a circular
scan pattern
PHL 1978-19, TNO, The Hague, Netherlands (1978).

[31] Ito, N. and Kimura, K.
Field experiment study on the convective heat transfer
coefficient of exterior surfaces of a building
ASHAE Trans. Vol. 78-1, (1970).

[32] Kowalski, G.J. and Mitchell, J.W.
Heat transfer from spheres in the naturally turbulent,
outdoor environment
J. of Heat Transfer (1976), p. 649.

[33] Šlančiauskas, A. and Pedisius, A.
Effect of free stream turbulence on the heat transfer
in the turbulent boundary layer
Sixth International Heat Transfer Conference, 2, 1978.

[34] Forthcoming report describing the 'HDS', an instrument measuring the shortwave- and longwave sky-radiance distribution.

[35] Wartena, L., et.al.
Opsporing van kwelplaatsen en zandbanen middels warmtebeelden 1979
Rapport RSWS 215, p. 19.

[36] Raithby, R.D. and Eckert, E.R.G.
The effect of turbulence parameters and support position on the heat transfer from spheres
Int. J. Heat and Mass Transfer, 11, 1968.

[37] Vos, J.C. de
The emissivity of tungsten ribbon
Thesis at the University of Amsterdam, 1953.

[38] Jong, A.N. de
Description of an infrared reflectometer
Forthcoming publication.

[39] Hudson, R.
Infrared system engineering
Wiley & Sons, 1969, London.

[40] Wartena, L., et.al.
Checking of some formulae for the calculation of longwave radiation from clear skies
Arch. Met. Geoph. Biokl., Ser. B, 21 p. 335-348, (1973).

[41] Wartena, L., et.al.
Het klimaat en de verdamping van een meer in centraal Iraq
Meded. Landbouwhogeschool, Wageningen, 1959.

[42] Wartena, L., et.al.

Some experiences on the measuring of longwave radiation
fluxes

Arch. Met. Geoph. Biokl. Ser. B., 14, 189 (1966).

ACKNOWLEDGEMENTS

The work presented in this thesis is carried out in the framework of project A72/KL/026 of the Physics Laboratory TNO. I am grateful to all members of the Infrared Group and without detracting anybody I would like to mention Teun Liedorp for building the complicated electronics and Peter Fritz for his assistance during installation in the field.

It is a great pleasure to thank professor L. Wartena for his stimulating interest and cooperation and I also wish to thank professor J.A. Wisse for his criticism during the last stages of this work.

Invaluable assistance has been obtained from the reproduction department of the Physics Laboratory TNO in the preparation of this booklet. Many thanks go to Fred Meijer and his coworkers in particular Monique van Stuyvenberg for typing, Hans Mazer for the photographic reproduction, Gerard Mooij for the drawings and Hans van der Laan for the final printing.

I credit my coffee-machine for keeping me awake during late evenings (night) work.

I deeply admire my parents for the way they guided (guarded) my life and for the way they raised their children.
To both I dedicate this thesis.

CURRICULUM VITAE

Pieter Jacobs was born in 1949 in Groesbeek, a beautiful village, located near Nijmegen. He received his elementary and highschool education in Beek and Nijmegen. He studied physics at the Technological University of Eindhoven from 1968 until January 1973; during the candidate work no particular choise was made, however a slight tendency was observed to theoretical work in the field of heat- and mass transfer. Doctoral work was involved with heatlosses in a Helium 3/4-cooler and the measurement of especially low temperatures (paramagnetic demagnetization).

Having completed his college education Uncle Sam 'asked' for a voluntarily contribution to serve his purposes. After ten months of a rather cheerful life he joined the Infrared Research Group of the Physics Laboratory TNO in Den Haag in the summer of 1975. From the beginning work was concentrated on thermal behaviour of backgrounds and objects related to infrared detection/recognition. After several years of working in this area, ideas about theory and experiments became more clear and eventually lead to the results presented in this thesis.